Available online at www.sciencedirect.com
SCIENCE DIRECT®
Icarus 172 (2004) 104–126
ICARUS
www.elsevier.com/locate/icarus

Cassini VIMS observations of the Galilean satellites including the VIMS calibration procedure

T.B. McCord [a,b,*], A. Coradini [c], C.A. Hibbitts [b], F. Capaccioni [o], G.B. Hansen [b], G. Filacchione [o], R.N. Clark [d], P. Cerroni [o], R.H. Brown [e], K.H. Baines [f], G. Bellucci [c], J.-P. Bibring [g], B.J. Buratti [f], E. Bussoletti [h], M. Combes [i], D.P. Cruikshank [j], P. Drossart [k], V. Formisano [c], R. Jaumann [l], Y. Langevin [g], D.L. Matson [f], R.M. Nelson [f], P.D. Nicholson [m], B. Sicardy [k], C. Sotin [n]

[a] *HIGP/SOEST, University of Hawaii, POST 502, Honolulu, HI 96822, USA*
[b] *Planetary Science Institute, 22 Fiddler's Rd., Winthrop, WA 98862-0667, USA*
[c] *Istituto Fisica Spazio Interplanetario, CNR, Via Fosso del Cavaliere, Roma 00133, Italy*
[d] *USGS, Mail Stop 964, Box 25046, Denver Federal Center, Denver, CO, USA*
[e] *Department Pl. Sci. and LPL, University of Arizona, Tucson, AZ 85721-0092, USA*
[f] *Jet Propulsion Laboratory, Pasadena, CA 91109, USA*
[g] *Université de Paris Sud-Orsay, IAS, 91405 Orsay Cedex, France*
[h] *INAF Osservatorio Astronomico di Capodimonte, Napoli, Italy*
[i] *Departement de Recherche Spatial, 5, Place Jules Jannsen, 92195 Meudon Principal Cedex, France*
[j] *NASA Ames Research Center, Astrophysics Branch, Moffett Field, CA 94035-1000, USA*
[k] *Observatoire de Paris-Meudon, 5, Place Jules Jannsen, 92195 Meudon Cedex, France*
[l] *DLR, Institute for Planet. Expl., Rutherfordstrasse 2, D-12489 Berlin, Germany*
[m] *Cornell University, 418 Space Science Bldg., Ithaca, NY 14853, USA*
[n] *University of Nantes, B.P. 92208, 2, rue de la Houssinière, 44072 Nantes Cedex 3, France*
[o] *Istituto Astrofisica Spaziale e Fisica Cosmica, CNR, Via Fosso del Cavaliere, Roma 00133, Italy*

Received 8 June 2003; revised 31 May 2004

Available online 26 August 2004

Abstract

The Visual and Infrared Mapping Spectrometer (VIMS) observed the Galilean satellites during the Cassini spacecraft's 2000/2001 flyby of Jupiter, providing compositional and thermal information about their surfaces. The Cassini spacecraft approached the jovian system no closer than about 126 Jupiter radii, about 9 million kilometers, at a phase angle of $< 90°$, resulting in only sub-pixel observations by VIMS of the Galilean satellites. Nevertheless, most of the spectral features discovered by the Near Infrared Mapping Spectrometer (NIMS) aboard the Galileo spacecraft during more than four years of observations have been identified in the VIMS data analyzed so far, including a possible ^{13}C absorption. In addition, VIMS made observations in the visible part of the spectrum and at several new phase angles for all the Galilean satellites and the calculated phase functions are presented. In the process of analyzing these data, the VIMS radiometric and spectral calibrations were better determined in preparation for entry into the Saturn system. Treatment of these data is presented as an example of the VIMS data reduction, calibration and analysis process and a detailed explanation is given of the calibration process applied to the Jupiter data.
© 2004 Elsevier Inc. All rights reserved.

Keywords: Satellites; Galilean satellites; Jupiter system; Satellite surfaces; Surface composition; Space mission

1. Introduction

The Visual and Infrared Mapping Spectrometer (VIMS) (Brown et al., 2004) is part of the instrument payload on

* Corresponding author. Fax: +509-996-3772.
E-mail address: mccordtb@aol.com (T.B. McCord).

0019-1035/$ – see front matter © 2004 Elsevier Inc. All rights reserved.
doi:10.1016/j.icarus.2004.07.001

the Cassini–Huygens spacecraft that flew by the Jupiter system in December 2000 on its way to orbit the Saturn system in early July 2004. The VIMS acquired measurements of the four Galilean satellites, in addition to other observations, over a period of several months (Brown et al., 2003). The spacecraft approached the jovian system no closer than about 126 Jupiter radii, about 9 million kilometers, and a phase angle of $< 90°$, resulting in only hemispheric, subpixel, observations by the VIMS of the Galilean satellites. These observations are much lower in spatial resolution but are higher in spectral resolution and coverage and in signal-to-noise ratio than the previous Galileo NIMS observations. In some cases the VIMS observations cover different sides of the satellites or different phase angles and, of course, at different times than seen before. Thus, as part of the VIMS data science analysis, it is useful to compare the VIMS findings with the earlier NIMS results. Further, the Galilean satellite observations are part of a broader radiometric calibration effort that began before launch (Brown et al., 2004). It will be useful for future analysis efforts to describe here the procedures and results in improving and applying the spectro-radiometric calibration and present an example of analysis of VIMS data in anticipation of the efforts expected for the Saturn system data.

2. Instrument characteristics

VIMS consists of two integrated, bore-sighted slit-grating spectrometers with separate reflecting telescopes (Brown et al., 2004). These two spectral channels cover the ranges 0.35–1.05 μm (Visual channel) and 0.8–5.1 μm (IR channel) with nominal spectral sampling of 7.3 nm (96 bands) and 16.6 nm (256 bands), respectively. The VIMS Visible (V) and Infrared (IR) spectral channels have different fore optics and types of focal planes (detectors) and they produce data sets with different characteristics and have different calibrations. VIMS-V is equipped with a frame transfer 256×512 pixels CCD matrix detector on which spatial and spectral information are simultaneously stored. Radiation collected from VIMS-V telescope is focused onto the spectrometer slit. The slit image is spectrally dispersed by a diffraction grating and then imaged on the CCD. Thus on each CCD column is recorded the slit image at a given wavelength band. The slit long axis lies in the cross-track direction of the S/C motion; the full 2D image is then built by mirror scanning in the along-track direction. The IR channel has a one-dimensional focal plane and scans its IFOV in two dimensions: along and perpendicular to the slit's long axis. The VIMS-V has two spatial resolution modes, 167×167 and 500×500 μrad per IFOV; the VIMS-IR has two modes of 250×500 and 500×500 μrad per IFOV. The measurement modes of these two channels are defined so as to produce compatible data sets that can be used to create a single data cube covering the entire spectral range. This is achieved by operating both instruments in the 500×500 μrad mode. To achieve this the IR channel co-adds two 250×500 μrad IFOVs while the V channel integrates three 167×500 μrad IFOVs. Both channels operate with the same spectral sampling (7.3 nm/band for V and 16.6 nm/band for IR) independent of the spatial resolution used. Nevertheless, for clarity we will separately treat the analysis for each of the two spectral channels.

The nominal data set is an image cube consisting of two spatial dimensions and one spectral dimension. Because the IR portion of the instrument collects one IFOV per mirror step in its cross-track direction, it drives the rate at which an image cube is acquired when the visual and IR channels are simultaneously operated.

The integration times are coordinated for the V and IR channels within operational constraints so as to achieve the desired DN signal levels. The V channel, with its two-dimensional array detector, acquires in one exposure (integration time) all spectral channels for the entire line of pixels, (nominally 64) along its slit projected onto the source target. The IR channel, with its linear array detector, integrates and reads out its detector 64 times while moving its IFOV, using the IR telescope's scanning secondary mirror along the IFOV of the V channel slit, to obtain data for all 64 nominal pixel positions along the V-channel slit. The VIMS V and IR are bore-sighted and are normally synchronized so that the V channel exposes simultaneously for an entire IR line when the IR channel is scanning the same line, making the two channels of observations simultaneous for a line (there is in fact a small offset in the bore sights of the two channels of between 1 and 2 pixels).

The data returned by the VIMS consist of raw data numbers for each spectral channel at each spatial pixel. Each spectral channel is assigned a wavelength determined from the wavelength calibration, and the data numbers, once the dark and background signal have been subtracted, are multiplied by a radiometric response function for each pixel that relates raw instrument response in DN to physical units. The radiometric response function is derived from measurements made on the ground before launch, enhanced with in-flight measurements of Venus, the Moon, Galilean satellites, and several stars. The resulting radiance can be divided by the solar flux to derive reflectance as a function of wavelength for the illuminated portion of the field of view. If other radiation is present, such as for Io and the Moon, the ratio will contain a mixture of thermal radiation by the target and reflected solar radiation at longer wavelengths. Deconvolution of emitted and thermal radiation from the target requires additional information potentially complicating the derivation of I/F values from the raw instrument response (Clark and McCord, 1980).

The Galilean satellite observations presented here were obtained while the spacecraft stared or 'pointed' at each object during Cassini's flyby of Jupiter in December 2000. Additional serendipitous satellite observations occurred when a satellite would pass through the VIMS FOV during 'pointed' Jupiter observations. In these instances, only satellites

that orbited within the full field of view of VIMS (32 mrad by 32 mrad) and near Jupiter were observed (mostly Io and Europa). The distance of the Cassini spacecraft from the Galilean satellites was such that the IR channel observations of the satellites were sub-pixel, which is true for all star observations as well. At Cassini's closest approach to Jupiter, Callisto came closest to filling the IFOV, with the angle subtended being ~ 0.51 mrad, about the same size as the 0.5×0.5 mrad IFOV of the nominal VIMS pixel. But the $\sim 70°$ phase angle of that observation results in the illuminated portion of Callisto being sub-pixel. The sub-pixel nature of all VIMS observations of the Galilean satellites has implications for the radiometric and spectral responses of the spectrometers for these objects. For the V channel, the slit width is 1/3 that of the IR channel, thus, the satellite images were sometimes larger than the V slit. Nevertheless, the instrument was operated in the 500×500 μrad spatial resolution mode, to obtain a uniform data set for VIMS V and IR, resulting effectively in sub-pixel observations for the VIMS-V instrument as well.

Observations of the satellites were made throughout the several phases of the encounter (Brown et al., 2003). Used in this analysis are those observations made when the angle subtended by the satellite was at its maximum (closer to Jupiter encounter) and the greatest part of the visible satellite hemisphere was illuminated (smaller phase angles). These are measurements from targeted observations during the Phase B, C, D, and E portions of the encounter, just before and after closest approach, and with phase angles varying from $\sim 20°$ to $\sim 90°$. The longitudinal coverage for the returned observations of the satellites includes both the leading and trailing hemispheres of Io and Ganymede, but only the leading hemisphere of Europa for the IR channel (due to spacecraft pointing restrictions and spacecraft operations problems causing loss of planned observations). For the photometric analysis a slightly larger data set, which includes both leading and trailing hemisphere of Europa, has been used for the VIMS-V channel. In addition, some data near closest approach to Jupiter were lost due to a spacecraft saving event.

3. Data characteristics

The icy Galilean satellites are a challenge to observe in the infrared because of the reflectance characteristics of H_2O. Ice and heavily hydrated materials absorb strongly beyond a wavelength of about 2.5 μm, but have higher reflectance shortward of about 1.3 μm and between the several strong vibrational absorptions between 1.3 and 2.5 μm. This effect on the signal obtained for the icy Galilean satellites is enhanced because solar radiation and instrument sensitivity are greater at shorter wavelengths. Thus, for our observations of the Galilean satellites at least two integration times were employed to acquire high SNR data for the entire IR spectral range. A similar challenge exists toward the UV region, due to the presence of sulfur and other UV-absorbers, for all the satellites' spectra where the solar flux, satellite reflectances and instrument response all decrease.

Example DN spectra for a set of coordinated observations of Ganymede by VIMS V and IR are shown in Fig. 1. Results for two integration times are shown. The IR-channel spectra for the longer integration time (636 ms) have higher DN values and saturate at some of the shorter IR wavelengths, as expected, but possess adequate SNR for detecting absorption features at longer wavelengths. Shorter integration time observations (here, 156 ms) do not saturate at any wavelength for any of the satellites and are thus scaled and substituted for the shortwave saturated portion of the longer integration time observations. Note that in Fig. 1 the IR channel DN values for the longer wavelength channels are scaled upward by a factor of 20 to better show the nature of the spectra.

There are three spectral channel groups in the IR domain in which a few pixels have low sensitivity (detectors: 142 to 144, 223 to 225, 276 to 278). These correspond to areas of the detectors where the order sorting filters, placed over the detector array, abut and obscure greater amounts of light (Brown et al., 2004). The signal response of the detectors at these filter overlap areas is non-linear with integration time and signal, making the absolute calibration of these detectors difficult or impossible. There is one such filter interface for the V channel as well, located at channel 35.

There is a wavy pattern in the IR instrument response, most evident in the second spectral channel range (detectors 144 to 223). It is inferred that the associated order-sorting filter creates interference patterns (a Fabry–Perot effect) on the detector. This effect is present in observations of both resolved and unresolved objects and appears to be consistent. Thus, we treat this effect as part of the radiometric calibration, although some dependence on the target observed might be expected. The sharp drop in signal near channel 220 is due to the drop in reflectance of the satellite surface caused by the H_2O molecule.

There are single-pixel, single-spectral channel deviations in the data that we call "spikes" (e.g., in Fig. 1 near channel 54 and especially longward of channel 278 where the signal is particularly low). These are due partly to particulate radiation from the spacecraft nuclear power generators and from cosmic rays striking the detectors, and cannot be calibrated. Instead, we have developed algorithms to detect and remove them. In addition, in the V and IR channels, there are several detector pixels that have higher than average dark current, but their characteristics are known and linear and the effect is removed in the calibration process.

4. The infrared channel data reduction

The IR channel observations used in this analysis (Table 1) are all pointed observations of individual Galilean satellites. That is, the spacecraft was commanded to point to a specific location, and the spacecraft did this very well it

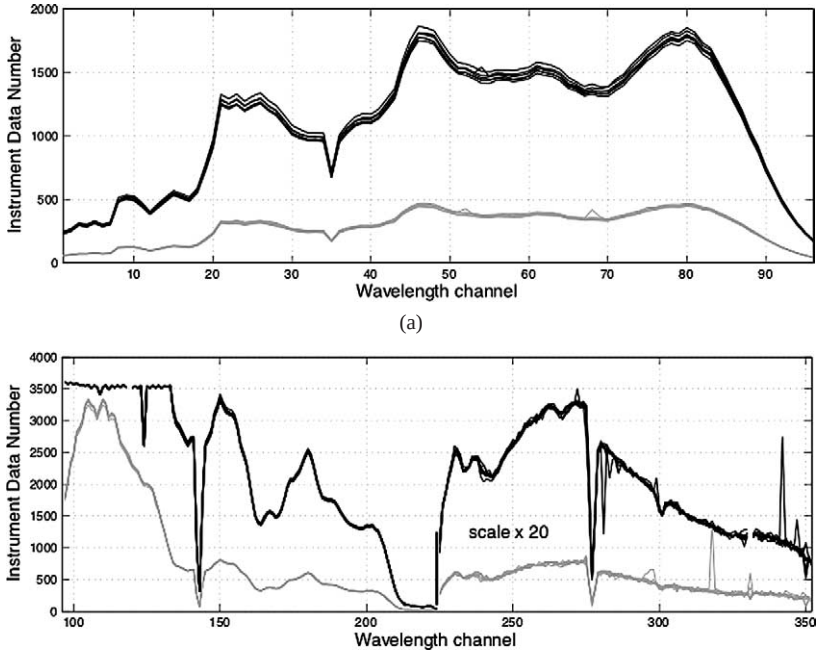

Fig. 1. The DN spectra are for seven repeated sets of Ganymede observations taken on Day 364, 2000, with integration times of 156 ms (gray) and 636 ms (black) for both the (a) visual and (b) IR channels. This series occurred just before closest approach, yet Ganymede is slightly sub-pixel to the IR channel. The phase angle is near 70°, and the effective central longitude is ∼ 020°. The signal in shortwave portion of (b) at the longer integration time is saturated from channel 97 to 133. Although VIMS V and IR use 12-bit digitization, and can record up to 4095 data numbers, saturation occurs at ∼ 3550 DN for the IR channel because the background-subtracted signal is displayed. The visual channel does not saturate for these measurements, even at the longest integration times.

Table 1
Characteristics of the Cassini VIMS pointed Galilean satellite observations used in the VIMS IR channel analysis

Object (year)	Time (Julian Day, Time)	# of obs. used	Phase angle	Sub S/C longitude
Io (2000, 2001)	364T0905-0915	3	∼ 70	300 (325)
	364T1120-1124	4	∼ 70	315 (340)
	366T0305-0335	6	∼ 70	285 (305)
	366T0550-0605	4	∼ 70	315 (335)
	001T0020-0045	25	∼ 90	300 (320)
Europa (2000, 2001)	348T0535-0800	18	0.4–0.6	16–26
	364T0800-0830	21	∼ 70	150 (175)
	366T615-0700	10	∼ 70	340 (360)
	010T1035-1055	29	∼ 90	190 (230)
	012T0600-2300	30	∼ 90	061 (110)–132 (180)
Ganymede (2000, 2001)	364T0650-0720	21	∼ 70	355 (020)
	010T0945-1030	24	∼ 90	190 (230)
Callisto (2000)	349T2000-0715	12	Pass through 0	326–334

seems. For these, the sub-pixel object was located in nearly the same place (apparently within a few 10ths of the slit width and pixel) in the IR spectrometer aperture and thus the IR spectrometer response is expected to be nearly the same for all these sub-pixel observations.

The usual procedure is to treat the DN data to a series of processes, including to dark/offset and spike removal and then to spatial, spectral and radiometric calibration. The spatial calibration involves using the results of ground point source and inflight star measurements over the FOV to correct for aberrations in the optical system and to relate the focal plane to far field geometry. There is also the flat field calibration that adjusts all pixels across the FOV to the response of the bore sight pixel. In this VIMS IR channel Galilean satellite case, there is no spatial or flatfield calibration needed, as all satellites were effectively only sub-pixel point sources appearing in the same IR pixel. The spectral and radiometric calibration is, however, especially complicated by the sub-pixel nature of the sources, as we discuss in detail here. The objective is to convert DNs to

radiance and then to reflectance by dividing by the solar spectrum.

4.1. Anomalies and artifacts in the IR data

We describe here the anomalies in the data. Some artifacts result from the sub-pixel nature of these observations. The spectral calibration and spectral resolution are controlled by the width and location of the slit, as projected by the spectrometer optics onto the detector. An object that subtends an angle smaller than that of the slit (the definition of sub-pixel) will act as its own slit and thus any movement of the object within the slit will affect both the spectral calibration and, if the detector response is non-uniform across its surface, the instrument response function. That is, the spectral resolution and wavelength calibration changes to what it would be if the slit were the width and at the location of the image, as projected onto the detector according to the instrument point spread function (PSF) at that location in the FOV and spectrum. As the object image formed by the foreoptics is moved around in the wider slit area at the entrance of the spectrometer, the dispersed image of the object projected by the spectrometer optics onto the detector moves around on the array of detectors. These effects result in a wavelength calibration dependent on the location of the sub-pixel object relative to the slit. For a point source the wavelength assignment could change as much as $\pm 1/2$ channel from that resulting when the slit is filled, assuming a perfectly focused system with a perfect PSF. In fact, the IR channel PSF varies across the FOV and spectrum from below half the pixel at the center of the detector array to approximately a pixel at the extreme ends of the FOV and spectrum. This means that the effect on the wavelength assignment to each spectral channel (spectral calibration) can vary as does the PSF across the spectrum and FOV, especially for sub-pixel sources. Star scan tests in flight across and along the slit suggest that most of the variation seen is due to the PSF moving through the slit and that any intrinsic variation in sensitivity across the detector pixels is not seriously affecting the signal.

This effect is mitigated by using only pointed observations, i.e., where the object is positioned and held at a fixed position in the field of view of VIMS during data acquisition. The accuracy and stability of this type of observation is limited by the spacecraft performance and appears to be close to 1/10 of a pixel, so that pointed sub-pixel target observations provide consistent spectra that can be calibrated. The consistency of pointed observations can be seen in plotting all the spectra from a series of repeated individual observations onto one plot (Fig. 1), which helps reveal anomalous signals (spikes) in individual spectra.

The same seven Ganymede IR DN spectra shown in Fig. 1 are shown in Fig. 2 on an expanded scale and separately for each of the four spectral segments between the low sensitivity pixels created by the detector filter gaps. Apparently random variations among the spectra at the 2 to 4% level are visible as are several spikes, especially in the low signal portion of the spectra beyond 2.8 μm. There also are some

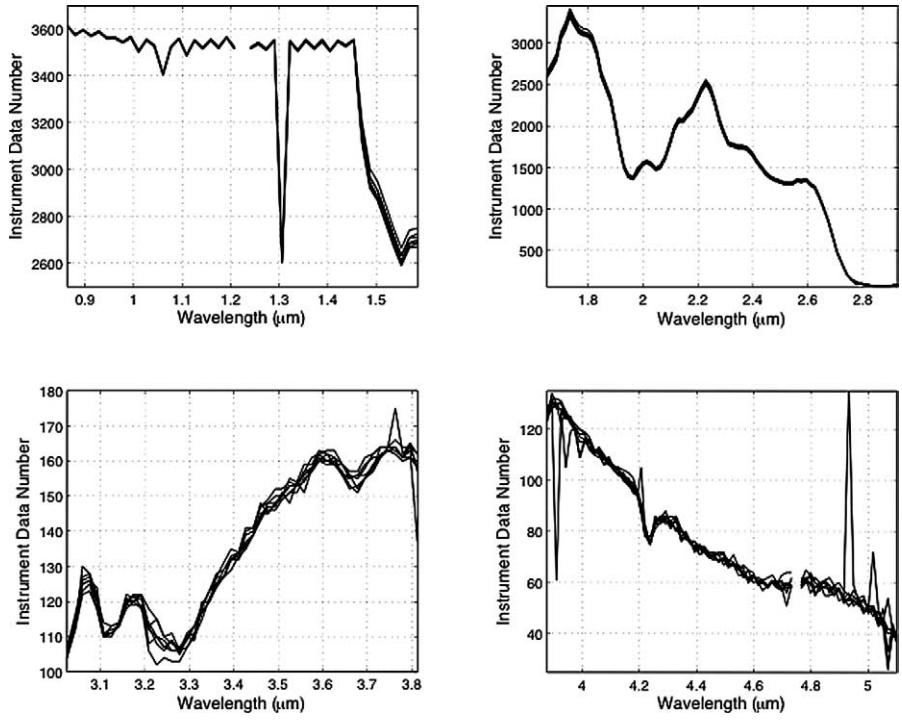

Fig. 2. The IR-only DN spectra for the same seven spectra of Ganymede as plotted in Fig. 1. Segments, bounded by the low-sensitivity pixels (corresponding to filter overlaps), are plotted separately to show detail. No processing other than subtracting instrument dark has been applied. The laboratory-derived wavelength-calibration file has been applied.

'odd–even' patterns evident, due to the sub-pixel nature of the source and detector/multiplexer readout effects.

In Fig. 3 are shown the DN spectra for the two longer-wavelength segments for Ganymede compared with similar spectra for Callisto, showing similar behavior. Noise spikes are especially apparent in the 3.5- to 3.7-μm region for the Callisto spectrum. In Fig. 2 an absorption at 4.23 μm is apparent, which clearly appears in the spectra of both Ganymede and Callisto in Fig. 3. This confirms the CO_2 absorption announced for Callisto by (Carlson et al., 1996) and described for Europa, Ganymede and Callisto (McCord et al., 1997, 1998a) using the Galileo NIMS data. The spectral channel-to-channel or odd–even channel variations in the DN spectra are evident in Fig. 3 and are particularly apparent for the two channels at the bottom of the CO_2 band in Fig. 3. Note that some spectra show the shorter-wavelength channel higher in DN while other spectra show the opposite. This is probably the effect of slight changes in position of the sub-pixel source within the IR spectrometer slit, causing the dispersed spectrum to shift slightly on the detector array and effectively changing the wavelength calibration of the spectrometer. Spectral channels near a steep rise or fall in the spectrum DN levels will show great sensitivity to the wavelength calibration used and to exactly where the spectral feature falls on the detector array. This effect, of course, is present throughout the spectrum for sub-pixel sources, but is most apparent at points where spectral contrast is greatest.

The formal channel-to-channel standard deviation from the average of these spectra in Fig. 3 for the 3.0- to 3.8-μm segment ranges from 3.6 to 16.9 DN (1.5 to 5.6%) for Callisto (not including the largest spikes) and from 0.5 to 8.1 DN (0.3 to 5.2%) for Ganymede. Note that the intrinsic instrument noise has been measured to be about ±0.5 DN, but the photon shot noise, assuming a 5% albedo for this longwave portion of icy Ganymede at high phase angle, is ±2 DN. Thus, the standard deviation for the spectra shown in Fig. 3 is only slightly larger than that expected. There are many possible sources for this slight excess in noise, including radiation spikes and slight movement in the source relative to the spectrometer entrance aperture from observation to observation.

The pointed observations of the Galilean satellites provide a unique opportunity to investigate the possibility of scattered light in the wavelength dimension. This can be a difficult phenomenon to detect in a mapping spectrometer designed around a linear detector array, such as the IR portion of VIMS. However, observation of Europa and Io provide an opportunity to detect scattering of light from shortwave to long (Europa) and from long wavelengths to short (Io). Europa is bright in the near IR because of its icy surface, which also makes its reflectance very low at mid-IR wavelengths (McCord et al., 2001). In contrast, eclipse observations of hot Io provide large signals at longer wavelengths, and little in the shortwave infrared. Figure 4 demonstrates that there is little or no scattered light detected in either di-

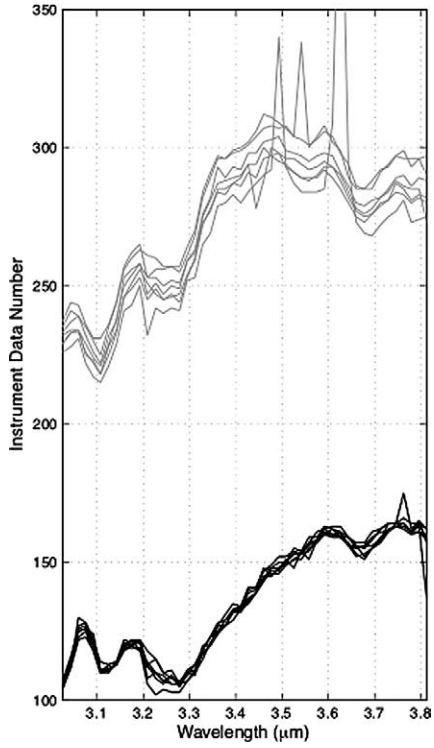

(a)

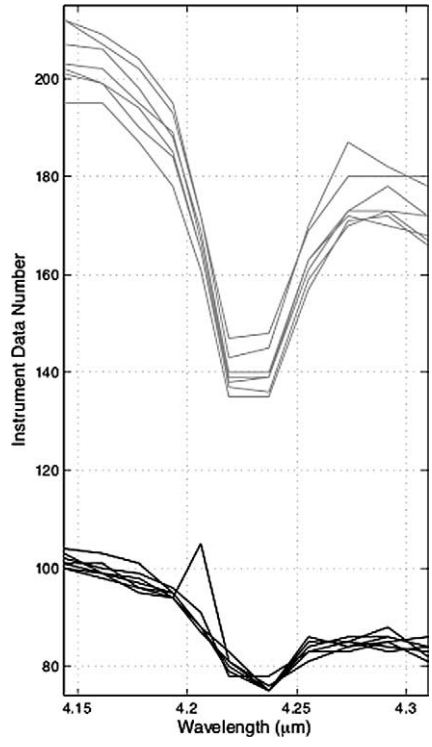

(b)

Fig. 3. Portions of the IR-only channels of the seven Ganymede (black) spectra from Fig. 1 as compared with the same spectral regions of a similar set of observations for Callisto (gray). (a) The Callisto spectrum contains some odd–even patterning in the 3.2- to 3.8-μm region. (b) Both the Ganymede and Callisto spectra show variations at the bottom of the ~ 4.25-μm CO_2 band for each moon. Laboratory wavelength-calibration file has been applied.

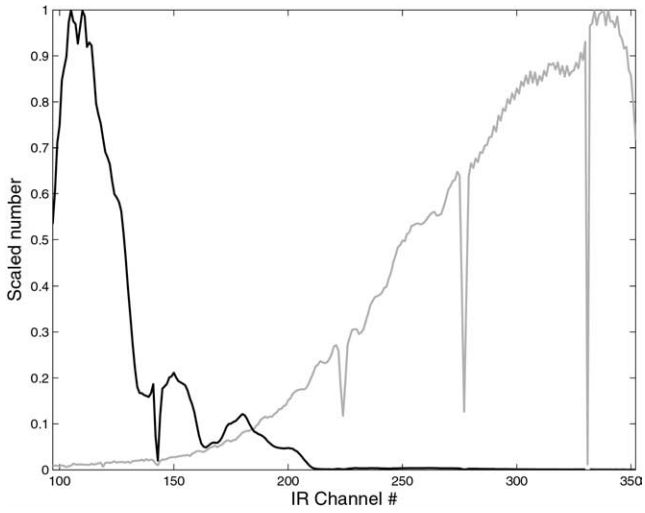

Fig. 4. VIMS IR DN spectra are shown for Io in eclipse (right) and for Europa (left). Both spectra have large amounts of signal at one end of the spectrum and very little at the other end. This suggests that there is none or very little light scattered across the spectrum.

rection in the wavelength domain, as the signal recorded in the dark regions is $< 1\%$ for the Io case (probably real signal from Io) and below system noise for the Europa case.

4.2. Preparing data for the calibration procedure

The first treatment of the "raw" DN spectra is to remove electronic offsets and background signals due to dark current and thermal background photons from the spectrometer optics. For the IR channel, a chopper is used as a no-signal source to enable measurement combination of "dark" offsets. The data returned from the spacecraft have a dark/offset signal already subtracted, but the subtracted signal is preserved in the data. Thus, the signal before dark/offset subtraction can be recovered and the dark/offsets can be analyzed. A more complete understanding of the nature of the dark/offsets can be obtained through dark sky measurements, called "background" rather than "dark." Because the IR chopper has a non-zero temperature it can contribute a measurable signal for long integration times at the longest wavelengths. This thermal contribution is either empirically determined from dark sky (background) measurements or modeled from an estimate of the chopper temperature and the assumption of a blackbody emission. Usually, the effect of the non-zero signal ($\leqslant 5$ DN for a 636 ms integration) from the chopper near 5 μm is removed before deriving the dark/offset-subtracted signal for the IR channels.

Following dark subtraction, radiation-induced spikes are removed. Our approach uses a direct averaging technique that relies on repeated spectra. Comparisons are made between spectra of a single object that were taken consecutively within minutes of each other and should ideally be identical. Deviations in spectra from the average are analyzed channel-by-channel with large deviations being removed before a new average is calculated. This technique avoids the need for cross-wavelength comparisons that are used when each spectrum is unique and that reduce the effective spectral resolution. For VIMS, the spikes always have positive DNs. If the spikes occur in the background (dark) measurement, however, after subtraction the spike will appear as a negative component in the resulting spectrum. Thus, both the background and the signal-filled pixel need to be "cleaned" of spikes. Essentially, many identical observations are averaged together and individual data points lying beyond a selected number of standard deviations from the average are removed. Then, the results are re-averaged and the data point removal criterion is tightened. This, of course, has the potential to miss-classify single event, single wavelength absorption or emission features as spikes, but no such event is expected to occur for the Galilean satellites.

For some data sets there is a weak odd–even pattern present, shown and discussed so far only for the 3.0–3.8-μm segment (Fig. 2). As stated earlier, this appears to be due to the sub-pixel nature of the sources and the variation of the PSF across the spectrum that change the wavelength calibration and cause slight differences between the general wavelength calibration used and detailed variations from spectral channel to spectral channel. The weak saw-toothed patterns are identified and the value of a single channel is replaced by an average of itself and the value of the channel at the next wavelength.

Finally, the displayed DN spectra for Callisto, Ganymede, and Europa (Fig. 5) and Io (Fig. 6) are the result of applying these corrections: dark/background subtraction, spike removal and odd–even patterning adjustment. Each spectrum is processed and the results are averaged. The observations used to create the average spectra in Fig. 5 and Fig. 6 are listed in Table 1.

4.3. The spectro-radiometric calibration procedure

The conversion of DNs to radiance (I/F) requires knowledge of the instrument spectral and radiometric response. The spectro-radiometric response function used here for the Galilean satellite observations was developed from a sequence of measurements starting with the ground calibration before launch (Brown et al., 2004; Capaccioni et al., 1998; Coradini et al., 2004) and progressing through the Venus flyby, the Moon flyby, several star measurements before and after the Jupiter encounter, and by using the known properties of the Galilean satellites.

None of these measurements provides a complete calibration due to various factors. For example, the IR channel's radiator cover had not yet been removed at the Venus flyby (as planned), and thus the IR channel was not functional. In addition, the IR signal was partly saturating during the Moon flyby due to the hot Moon and warm instrument radiator and optics (as expected), and observations of stars and satellites were sub-pixel. Nevertheless, using different sources and knowledge of these sources, a useful radiometric calibration function has evolved.

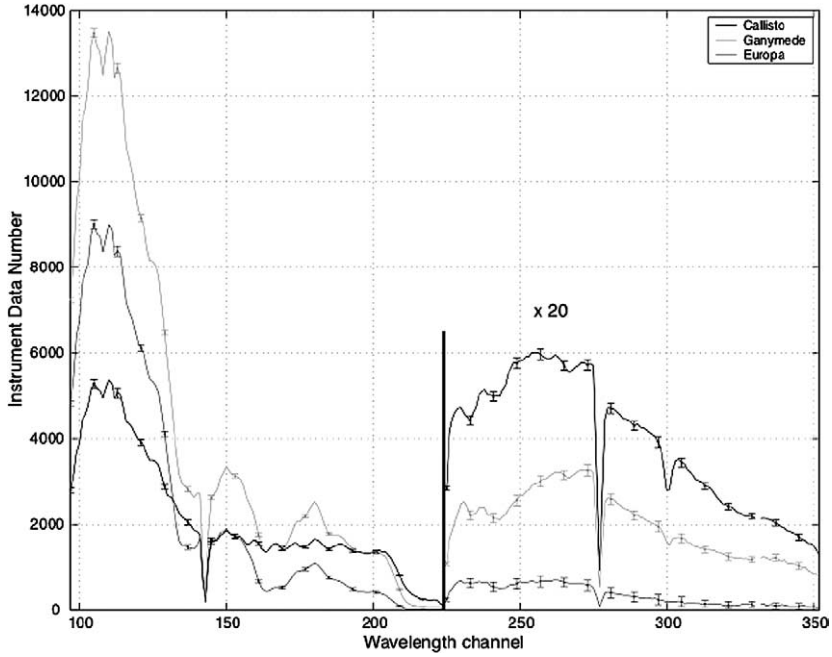

Fig. 5. The average spectra and 1-sigma error bars derived for each of the icy satellites: Callisto (black), Ganymede (light gray), and Europa (dark gray). Each spectrum (and error bar) has been multiplied by 20 at channels 225 and beyond, the spectral region where ice lowers the reflectance and the signal. Callisto is brightest in this region because it is the least icy. Although the visible and near infrared albedo of (icy) Europa is greater than Ganymede, Europa fills a smaller portion of the pixel, providing less light and therefore creating less signal in the instrument.

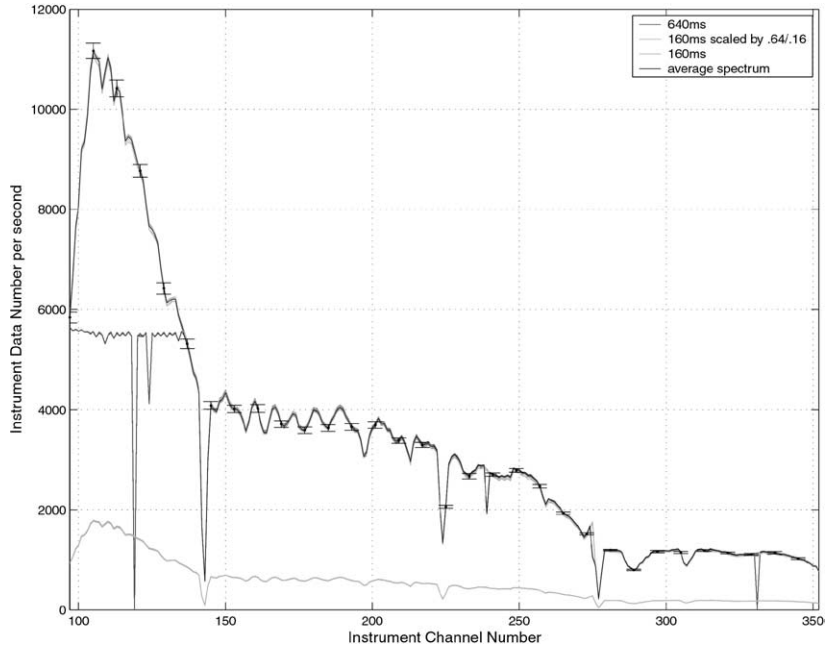

Fig. 6. The instrument response to reflected sunlight and emitted thermal energy from Io, for two series of observations at different integration times, plotted as DN/s. Six spectra each at 636 ms and 156 ms are used. Plotted are the average spectrum and 1-sigma error bars (black), the long integration time observations (black), and the 156 ms integration time observations (light gray). Also plotted, are the 156 ms integration time spectra (as DN) for comparison (light gray). Note that the two integration time observations (DN/s) overlap so completely at longer wavelengths that it is difficult to distinguish between the two sets of spectra. At long wavelengths, the 1-sigma error is approximately the width of the line.

The ground calibrations for the IR channel are discussed in Brown et al. (2004). Only a summary seems appropriate here as the purpose of this article is to present the Galilean satellite observations and, in the process, discuss the inflight calibrations. The IR VIMS was tested in a large vacuum chamber at the Jet Propulsion Laboratory by the science team before flight. The IR radiometric response first was measured using three sources: a tungsten lamp, a glow bar,

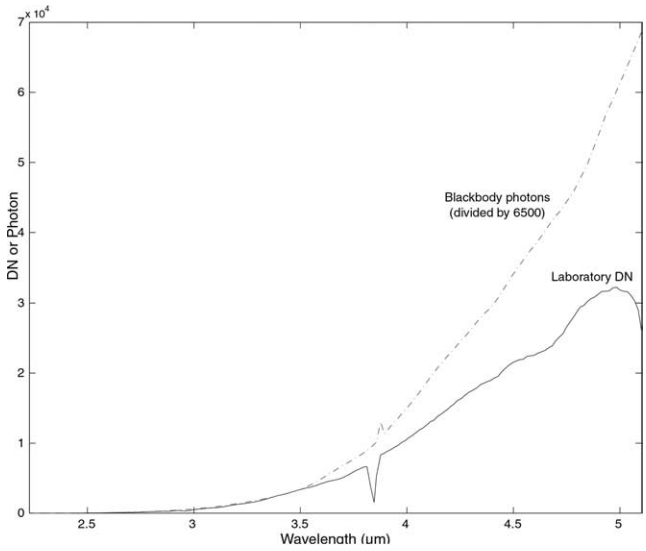

Fig. 7. The derivation of the longwave portion of the ground calibration using a 296.4 K blackbody. The photons are calculated using known instrument parameters and integration time applicable to the DN spectrum. The photon curve has been divided by 6500 for viewing purposes only. The ratio of the photon curve to the DN curve provides the radiometric calibration function. Low SNR limits its derivation to ∼ 3 μm.

and a blackbody cavity enclosing the entire FOV with no window. A monochrometer was used to measure the spectral passbands. After inflight measurements using the Moon and stars, it was determined that the tungsten lamp was malfunctioning and these measurements were not used. The 296.4 K blackbody cavity measurements (Fig. 7) proved to be superior to the glow bar measurements, due to higher SNR and more uniform FOV coverage, and were used as the basis for the long wavelength calibration, since augmented by the inflight calibrations.

Further measurements are required, of course, to substantiate and improve this calibration function. In reality, the radiometric calibration will require reanalysis throughout the life of the instrument and mission. Those attempting data analysis should be aware of the accuracy limits in calibration, and that instrument response changes may continue to occur for the life of the instrument.

The Moon observations were saturated at wavelengths shorter than 1.65 μm and longer than ∼ 4.1 μm even at the shortest integration times, due to the Moon being much brighter (hotter) than objects in the Saturn system, for which VIMS was designed, and the radiator and instrument optics being warmer than they are during operation at 10 a.u. and thus contributed significant thermal flux to the detectors. The star observations, besides being sub-pixel and subject to the problems previously described, are of low signal and of sources not well characterized at high-spectral resolution at the longer wavelengths. With the Jupiter system observations, another chance existed to improve the calibrations.

Between 1.65 and 4 μm, high-SNR spectra were obtained of the Moon at a spatial resolution sufficient to discern its mare and highlands, at a solar phase angle of ∼ 90°. By

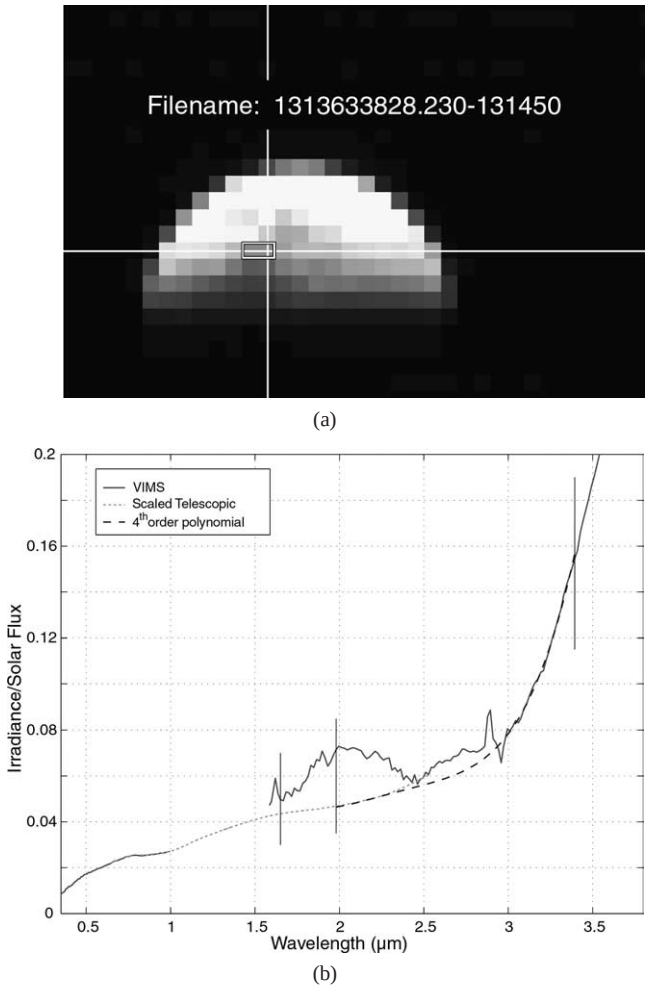

Fig. 8. (a) The image is from VIMS channel 200 (2.5594 μm) and is oriented with the North Pole to the right. The location of the two mare pixels are within the crosshairs and outlined by the box. (b) Derivation of the correction factor for the ground calibration using the VIMS-IR Moon observations. The correction factor is based on ground telescopic spectra (dotted line), and a 4th-order polynomial (dashed line). There is no VIMS data short of 1.65 μm or long of 4.1 μm (not shown).

comparing the observations of the lunar mare to the known spectrum of Mare Serenitatis (e.g., McCord et al., 1981) an improvement in the shape of the calibration curve and in the absolute level of the calibration were obtained in the visible and SWIR. An average DN for nearly identical mare regions identified in two pixels from 12 separate observations is used. The location of the two pixels in one observation is outlined in Fig. 8a. As the Moon moves only in the y-direction between observations, the locations of these two mare pixels in another observation is estimated by matching the DN from the pixels of this observation with the appropriate row in another observation.

We consider the spectrum of the Moon's mare to be smoothly varying throughout the infrared, thus the high-frequency variations in the laboratory-derived I/F are considered artifacts (Fig. 8b). These artifacts are removed by deriving a correction factor that is simply the ratio between

the smooth lines (considered to represent the actual lunar spectrum) and the I/F derived from the VIMS ground calibration. This correction factor is composed of 4 segments delineated in Fig. 8b by the black vertical lines. The ground calibration appears to provide valid relative radiometric calibration at wavelengths longer than ~ 3.41 μm (channel 251), where the ground calibration blackbody produced significant instrument response. However, for the VIMS IR I/F to match telescopic spectra at the short wave portion, a scaling factor of ~ 2.2 is required. From 1.9803 to 3.3937 μm (channels 165 to 250) the correction factor is derived for the region where the quality of the ground calibration effort suffered from low SNR. From 1.6507 to 1.9637 (channels 145 to 164) the telescopic spectrum is used as the true shape of the lunar spectrum. Since reliable VIMS-IR spectra from the Moon are not obtained shortward of the 145th channel, the correction factor for the 97th VIMS channel (the 1st IR channel) to the 144th is the same as for the 145th VIMS channel correction—i.e., the scaling factor of ~ 2.2.

The lunar-derived sensitivity improved the radiometric calibration, but refinement (and confirmation of the lunar-derived results) was achieved by comparing the VIMS-IR spectra to that of the Galilean satellites. We rely here on knowledge of the reflectance of each of the Galilean satellites (and also of Jupiter for the V channel) that has been derived from telescope observations (e.g., Clark and McCord, 1980; Calvin et al., 1995) and Galileo NIMS (Carlson et al., 1992, 1996; McCord et al., 1997, 1998a, 1999, 2001) to refine the relative radiometric calibration. Because the Galilean satellites are sub-pixel they are difficult to use to determine the absolute calibration. However, they have proven quite useful in calibrating the relative radiometric instrument response. Differences between the VIMS-derived reflectance spectra and those from NIMS and ground-based measurements are evaluated to determine their sources. In some cases, an adjustment in the VIMS calibration is made. This is the case, for example, when an unexpected spectral feature appears or a consistent difference from NIMS appears in the VIMS spectrum of all the Galilean satellites. The I/F calculated for each Galilean satellite using the ground and lunar-derived sensitivities are given in Fig. 9.

This improved calibration allows the comparison (Fig. 10) of the Io trailing hemisphere spectrum from VIMS and NIMS to show a disagreement in the wavelength channel assignments, especially in the SO_2 frost absorption bands. The current NIMS wavelength calibration was developed using detailed analysis of the NIMS data for Jupiter atmosphere and other sources with well-known absorption bands. In addition, the NIMS Io observations were checked using laboratory data for the SO_2 frost features. Evidence indicates that the VIMS wavelength calibration has changed since launch by about 12 to 22 nm. Another check of wavelength calibration can be made using the CO_2 band near 4.25 μm (Fig. 11). The VIMS band center is about 28 nm shorter than derived from NIMS (McCord et al., 1997, 1998a; Hibbitts et al., 2000, 2003), close to but not exactly the same as the offset derived from the Io observations. It is expected that there will be uncertainties at this level using these observations because the VIMS spectral channel width is about 16 nm (NIMS was 27 nm), and there are the wavelength calibration shifts associated with the sub-pixel nature of the Galilean satellite source and the variations of the PSF across

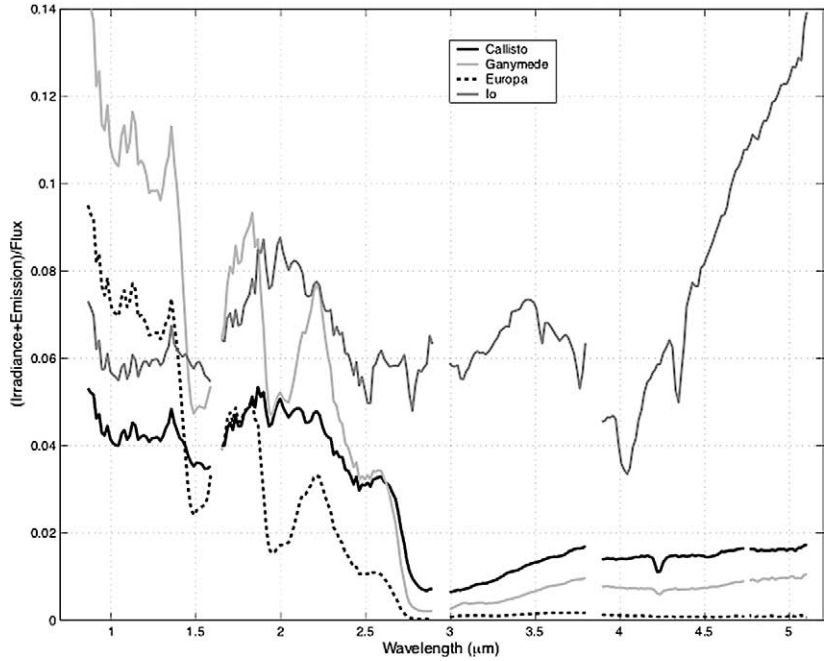

Fig. 9. The reflectance (I/F) spectra derived for the Galilean satellites: Callisto (black), Ganymede (light gray), Europa (dashed), Io (dark gray) using laboratory-derived radiometric sensitivity and wavelength calibration files. Note, the signal from Io is dominated at long wavelengths by thermal flux from volcanism and is not reflectance. Channels where order-filter overlap occurs (blank spaces in the spectra) do not respond linearly and are not plotted.

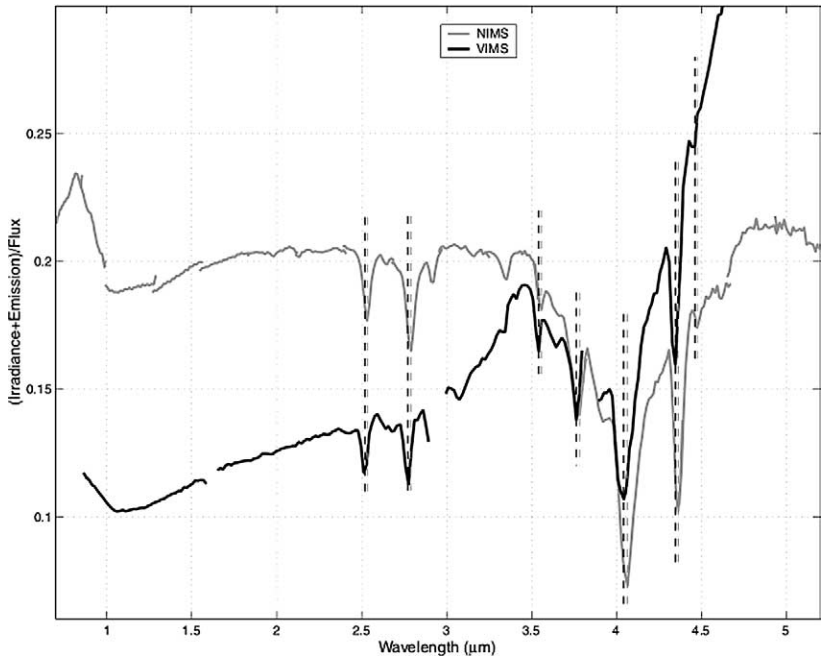

Fig. 10. The spectrum of the trailing hemisphere of Io as observed by the Near Infrared Mapping Spectrometer (NIMS) aboard Galileo is shown in gray. The VIMS spectrum, also of the trailing hemisphere, derived with the laboratory calibration, is shown in black, the bottom of the SO_2 ice absorption bands are consistently 12 to 22 nm shorter in the VIMS observation (dashed black) compared to the NIMS observation (dashed gray).

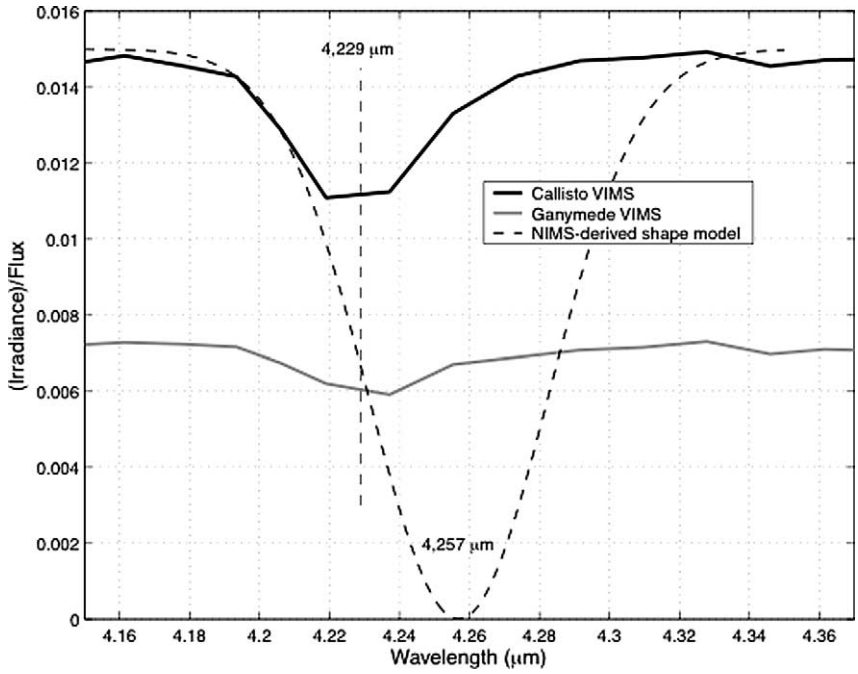

Fig. 11. The CO_2 absorption band as seen in the VIMS spectra of Callisto (black) and Ganymede (gray) compared to the shape model derived for the CO_2 absorption band on both these moons from many observations by NIMS. The VIMS band center appears to be $\sim$ 28 nm shorter than compared to NIMS.

the spectrum, as discussed above. The wavelength calibration for observations of Jupiter, a resolved object, shows a similar shift. Thus, we have calculated a new wavelength calibration. We recognize that this is somewhat circular, and we will use observations of objects in the Saturn system obtained after Cassini's arrival at Saturn to further improve the VIMS wavelength calibration.

The refinement of the radiometric calibration that was derived from the lunar results was an iterative procedure in which deviations from spacecraft (Galileo NIMS) spectra of each Galilean satellite were minimized. This procedure relies heavily on having high signal-to-noise observations of similar hemispheres of each satellite by both VIMS and NIMS. Because VIMS only obtained sub-pixel resolution,

NIMS reflectance spectra used for comparison were averaged to obtain an effective global reflectance spectrum. Of the VIMS observations, both 156 and 636 ms observations are used in order to obtain the highest signal level possible over the entire IR spectral range. Because the long integration time observations saturate at shorter wavelength (the water ice dominated spectra are brightest here), 156 ms observations are scaled to fill in this gap. The procedure begins with selecting stable VIMS observations for which corresponding NIMS observations exist, if possible. These occurred during Phase D and E of the Cassini Jupiter encounter, and tend to be of the trailing hemispheres. The VIMS spectra are first corrected for thermal emission from the chopper. A multi-order polynomial is fit to an average background-subtracted spectrum of deep space to derive the correction. For 636 ms observations, the effect is about 4 DN at 5 μm. This is a serious effect in spectra for both Ganymede and especially Europa where the DNs are less than 10 at 5 μm.

The individual spectra are then despiked. This was done by first scaling the spectra together at intervals defined by the filter overlaps to better distinguish noise from a single-channel spike. A single scaling function does not work for the entire wavelength range, but does work between the filter overlap regions. The scaling removes the DC offset between spectra that is likely due to movement of the satellite image within the spectrometer slit. The remaining variation appears to be random and is on the order of one or a few times of that expected for instrument noise. The spikes are removed if they are single-channel variations that exceed ~ 1.5 standard deviations of the mean. This technique has the potential to remove single-event, single-channel features that may be due to emission or absorption bands, but neither of these is expected to exist in IR data of the Galilean satellites. The spectrum of each satellite is again plotted in Fig. 12, this time with the improved calibrations.

5. The visual channel data reduction

In Table 2 are reported the satellite observations used in the analysis of the VIMS V channel. This list is different from the IR observation list reported in Table 1 because for the V channel we discarded all the observations with an integration time below 1 s, due to the low signal level. We also included observations in addition to the pointed observations to increase the phase coverage. In Section 2 we mentioned that the IR channel usually drives the observations. Nevertheless, the exposure time of the VIS channel is independently selected within a range whose upper limit depends on the exposure time selected by the IR channel. Thus, in several cases, the selected exposure time for the V channel might not have been adequate to achieve acceptable signal levels.

We have reanalyzed the Moon and Venus data to improve the existing VIMS V radiometric calibration, described in Brown et al. (2004). We were then able to define a more accurate instrument radiometric response. Among other advantages, this allowed us to derive the satellite absolute reflectances and albedos. As with the IR channel, the V radiometric calibration needs further refinements and improvements, which will be carried out throughout the life of the instrument.

It is worth noting that the V ground calibration effort was limited due to schedule problems. The ground calibration

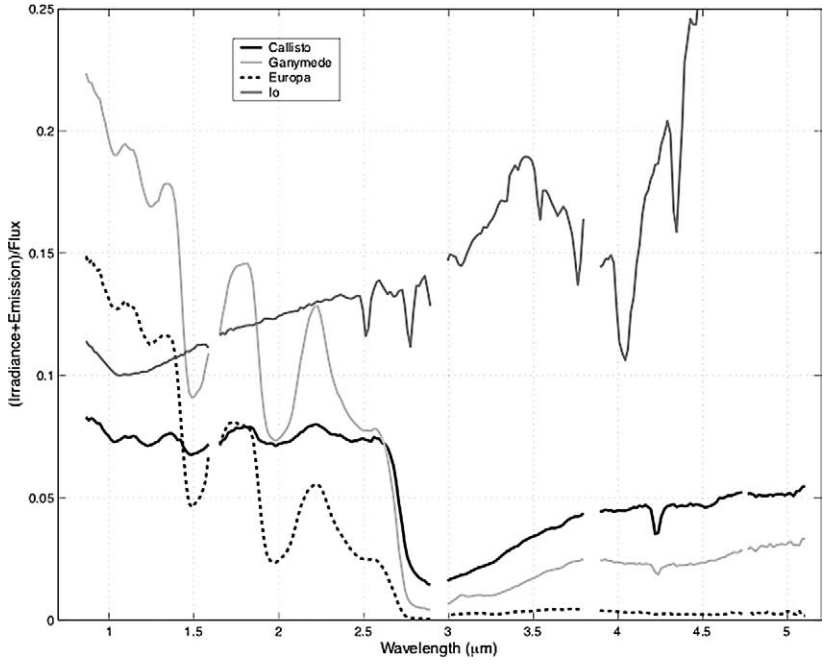

Fig. 12. New radiometric and wavelength calibration have been applied to the same DN spectra used in Fig. 9. Small irregularities remain at the few percent level.

Table 2
VIMS-V observations of the Galilean satellites used for the spectral analysis

Year-day-time	Io	Europa	Ganymede	Callisto	# of data cubes
2000-348T0541-0748		0.4°–0.6° 7.68			18
2000-364T0650-0716			52.5° 1.92–7.69		13
2000-364T0725-0752				45.5° 7.68	7
2000-364T0800-0827		56° 1.92–7.68			14
2000-364T0900-1100	52.1° 7.68 s				3
2001-002T0017-0040	77.3° 1.92–7.68				12
2001-002T1002-1006		76.9° 3.0			2
2001-006T0716			94.5° 40.0		1
2001-010T0948-1025			108.3° 3.84–7.68		16

data acquired have since been superseded by the inflight calibrations. However, a spare model of VIMS-V exists. This is a twin instrument assembled and tested by the prime contractor (Galileo Avionica) according to the flight instrument standards and with flight components. This spare is presently in the laboratory at IASF-Rome and is currently being used to characterize and possibly correct anomalous behavior identified during flight operations.

5.1. Anomalies and artifacts in the V data

As for the IR channel, spikes are frequently present in the V raw data due to high-energy particles impacts. Spikes affect only single pixels on the V two-dimensional array detector and are removed with algorithms that detect them (as for the IR channel), and then substitute the average DN value of the three-dimensional neighborhood pixels in the hyperspectral data cube. These spikes are randomly distributed over the CCD frame and affect both signal and background data.

The major instrumental anomaly detected in the V channel is the misalignment of the holographic grating with respect to the spectrometer's slit and CCD positions. According to the optical design, the grating's grooves should be placed perpendicular to the slit and to CCD columns direction in order to maintain the parallelism of the data cube. A small misalignment occurred during the assembly of the grating, but was not detected during ground procedures when the spectrometer and the telescope were co-aligned and focused. In the present configuration, the grating grooves direction is rotated from the ideal position. The rotation corresponds to an angle of about 3.12 mrad and its effect is to introduce a spatial shift of each monochromatic slit image on the detector array. The tilt was first detected during the analysis of the lunar observations data and has been subsequently verified on the spare model, allowing us to determine the cause.

The result of the mechanical rotation of the grating (tilt) is an image shift parallel to the slit direction, of about half a nominal pixel (500×500 μrad^2) between the first (350 nm) and the last (1050 nm) spectral channel. This tilt effect is particularly striking for sources with an angular width comparable to the instrument IFOV, such as for the Jupiter satellites and stars. For extended sources, the effect is evident for pixels at the targets edges, but it is not noticeable for fill pixels.

In general, short focal length imaging spectrometers like VIMS-V are not suitable for spectral analysis of sub-pixel/sub-slit targets. In these cases, the instrument response is different from that for extended sources and changes with the position of the object across the slit. The VIMS observations of the Galilean satellites are therefore at the instrument's capabilities limits.

In Fig. 13 are shown data from the seven pointed observations of Ganymede at a 7.68 s exposure. The figure shows two specific instrument characteristics. One is the discrete sampling of the instrument FOV by the CCD pixels. The satellite falls in between two pixels and consequently its flux is shared between the adjacent pixels A and B. From 500 nm longwards, however, the signal level for the two pixels changes, thus indicating a spectral tilt, which causes pixel B to have excess IR signal with respect to pixel A. Understanding this effect led us to a straightforward solution to overcome this problem for observations of small angular width sources (i.e., unresolved objects). Because the CCD pixels have a fill factor of 100%, no signal loss is expected between two adjacent pixels, and thus we can consider the sum of the DN signal from all the neighborhood pixels as the effective source signal. Because the normal mode of operation for VIMS-V is by summing on chip three spatial and five spectral adjacent pixels into one nominal pixel/resolution element, most all effects of sensitivity variation across a pixel are lost. In the case shown in Fig. 13, the total DN flux from Ganymede is the sum of the contribution from pixel A and from pixel B. This approach has been adopted throughout the analysis of the Galilean-satellite data and has proved effective.

For extended sources, however, the spectral tilt effectively slightly reduces the spatial resolution of the instrument. We are presently running laboratory tests using the flight spare V channel to better understand and compensate for this effect. The most likely solution would be to identify a de-tilting algorithm to correct the original data in specific cases, for example, analysis of surface regions where the spectral mixing could affect the identification of local compositional boundaries. The outcome of these laboratory tests, plus the analysis of extended sources, will be treated in a subsequent article.

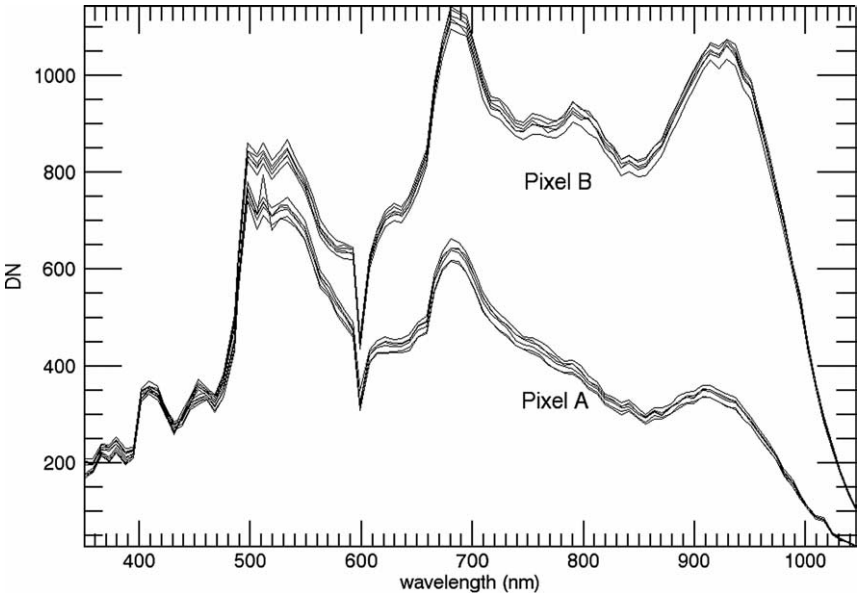

Fig. 13. Raw DNs for two Ganymede pixels (A, left side, B, right side) over seven consecutive observations. Pixel A collects mainly the blue part of the signal while pixel B the red part. This is a consequence of the tilt effect described in the text.

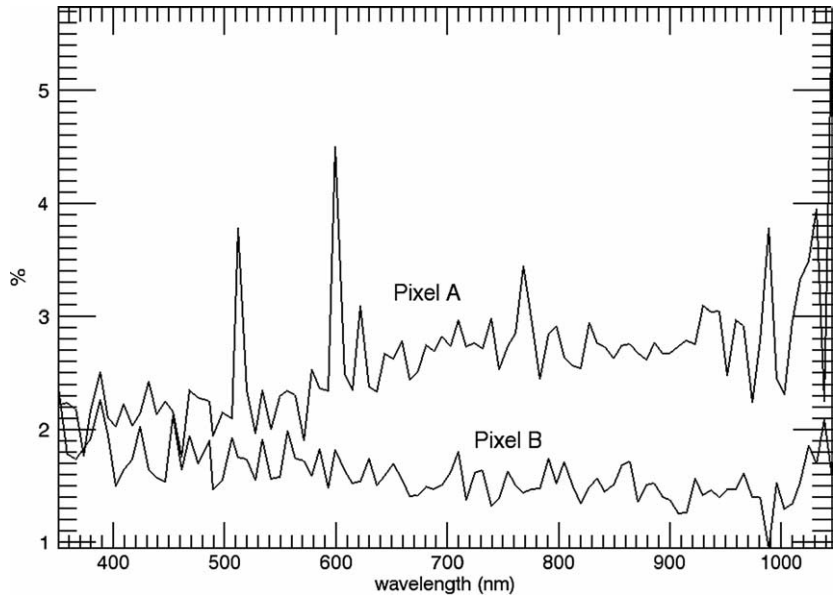

Fig. 14. Percentage contribution of the standard deviation to the signal in Fig. 13 for pixels A and B.

A final issue concerns the relative size of the Jupiter satellites with respect to the V slit. In contrast to the IR channel, the physical dimension of the V slit corresponds to 167 μrad; that is, the VIS channel has an intrinsic spatial sampling three times smaller than the IR channel. As mentioned before, to produce compatible data sets using the two channels requires the nominal mode of operation be with each V pixel a summation of three pixels in both spatial coordinates (along and across track). However, the IFOV by the V channel is 167 μrad wide, which implies that the observations of the Galilean satellites by the V channel are (barely) resolved. Thus, we do not expect any wavelength shift like those seen for the IR channel (see Section 4.1).

An analysis of the repeatability and noise characteristics of the data shown in Fig. 13, which can be considered typical for the other Galilean satellites, yields the result shown in Fig. 14, where we report the standard deviation of the co-added DN spectra. The intrinsic noise of the instrument as measured from background fluctuations is about ± 0.5 DN and thus the noise in the data is mostly photon shot noise.

5.2. Radiometric calibration of the VIMS visual channel

The main objective of the in-flight radiometric calibration was to calculate the instrument transfer function, or Unit Response, $\mathrm{UR}(s, \lambda)$, expressed in $(\mathrm{DN\ cm^2\ nm\ sterad})/(\mathrm{W\ s})$.

This allows a conversion of raw digital numbers to spectral radiance ($W\,cm^{-2}\,nm^{-1}\,sterad^{-1}$) for each pixel of the detector's frame placed at coordinate (sample, bands) $= (s, \lambda)$. Finally, by dividing this radiance by the solar radiance scaled at the Sun–target distance the I/F or the target spectral reflectance $\rho(\lambda)$ is obtained. For extended sources the $\mathrm{UR}(s, \lambda)$ can be expressed as:

$$\mathrm{UR}(s, \lambda) = \frac{\mathrm{DN}(s^*, \lambda)}{\rho(\lambda)\mathrm{SR}(\lambda)t_{\mathrm{exp}}}\mathrm{Flat}(s, \lambda), \quad (1)$$

where $\mathrm{DN}(s^*, \lambda)$ is the raw instrument output in DN for the pixel at spatial location s^* and at wavelength λ, $\mathrm{SR}(\lambda)$ is the Solar Radiance measured at mean Earth–Sun distance (1 AU) and scaled at the Sun–target distance (in AU), $\rho(\lambda)$ is the target spectral reflectance and t_{exp} is the integration time in seconds. $\mathrm{Flat}(s, \lambda)$ is a multiplying coefficient which corrects for instrument response non-uniformity at the spatial location s respect to s^*.

The other spatial variable, representing the third coordinate of the image cube, is associated with the mirror scan. Each instantaneous data set (frame) is associated with a scan position. Several in-flight tests have demonstrated that the UR does not depend on the scan position and a recursive application of the above formula to each instantaneous acquisition will provide a calibrated data cube. The electronic offset, dark and background contributions are removed from the signal DN as a preliminary step. The subsequent step is to remove all the spikes in the data. This is achieved using an automatic procedure that consider a three-dimensional neighborhood of each pixel and compares the central pixel value to the average value of the neighborhood. If the individual pixel DN exceeds a selectable threshold level, its local value is substituted with the neighborhood average.

The instrumental spectral characterization was performed during on-ground calibrations (Capaccioni et al., 1998) and continuously checked in flight by using the internal calibration unit. From these measurement we derived that at the nth band is associated the wavelength (in nm): $\lambda(n) = 353.33 + 7.33 \cdot n$.

From Eq. (1) the determination of the instrument transfer function can be split into two separate and independent steps:

- determine the flat field response of the instrument;
- determine a spectral calibration at a specific spatial point s^*.

5.3. Flat field

The first step of the radiometric calibration was to determine the pixel-to-pixel variation in the overall instrument response to a uniform extended source. Venus cloud tops at the spatial resolution of the encounter (17 km/pixel in nominal mode) represented spatially homogeneous and featureless targets, and thus were optimal sources for flat fielding.

The cube V1308947365 ($t_{\mathrm{exp}} = 50$ ms, acquired at 1999-175T20:23:08:08.384), corrected for dark and background signal, was used to define the pixel-to-pixel sensitivity variations. The result in Fig. 15 shows the percentage variation of the signal over the CCD frame (samples along x axis and bands along y axis) with respect to the center of the slit (sample 32). A detailed discussion of the nature of the features visible on the flat field is outside the scope of this paper and will be the subject of a subsequent publication. Nevertheless, we briefly state that the main cause of pixel-to-pixel variation is not the CCD itself (for which measurement of the non-uniformity yielded maximum variation of 1%) nor the tilt effect, but the overall optical system, especially the grating design. From a detailed analysis of Fig. 15 we derive that the maximum non-uniformities over the CCD frame are in the range $\pm 15\%$, with about 85% of the CCD frame falling in the range $\pm 5\%$. The final result is a matrix of multiplying coefficients $\mathrm{Flat}(s, \lambda)$, which is then used in Eq. (1).

5.4. Radiometric calibration

The next step is to identify a reasonable source of known reflectance to be used as an "absolute calibration spectrum." The absolute calibration of the V boresight pixel is then extended to the rest of the field of view using the flat field matrix.

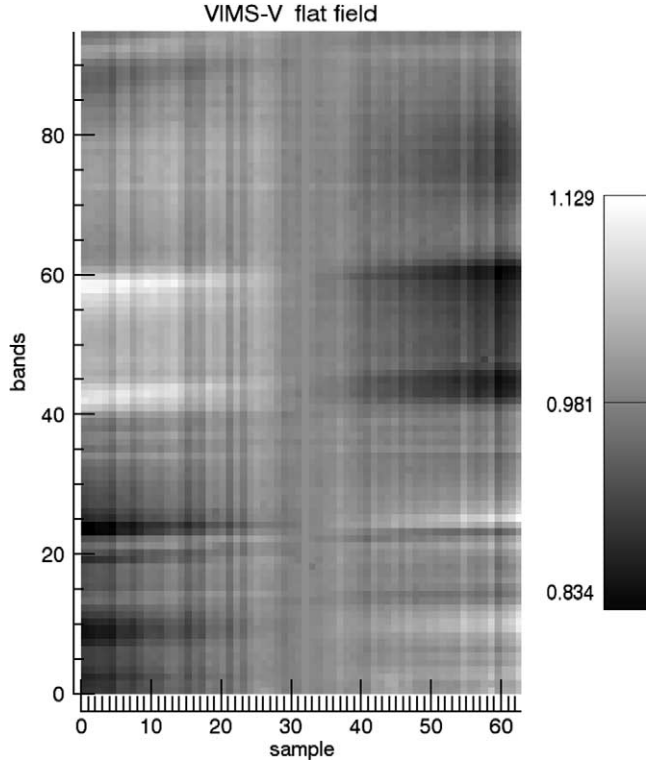

Fig. 15. Flat field image over the CCD frame normalized with respect to the slit's center (sample 32). The x axis represents the spatial coordinate along the slit, while the y axis corresponds to the spectral bands. A vertical line corresponds to the spectrum (from UV at bottom to IR at the top) of a single pixel on the slit.

In recent years, observations of the Moon were routinely used by several spaceborne multispectral imagers to provide a calibration reference (McEwen, 1996; Murchie et al., 1999). The main advantage lies in the fact that the Moon is the only atmosphereless body in the Solar System for which pristine material collected at well-known locations has been returned to Earth and analyzed in the laboratory (McCord et al., 1981; Pieters, 1999). The laboratory measured reflectance of the samples taken from the Apollo 16 landing site was used as our reflectance standard to derive a radiometric calibration function.

The first Moon data set returned by the V channel was obtained during Cassini's August 17, 1999 flyby of the Earth. During the flyby, Cassini was 385,000 km from the Moon, hence the spatial sampling in the nominal mode (IFOV of 500 μrad) is 192 km/pixel. We used the cube 1313633953.QUB acquired at 1999-230T02:12:25.498 with an exposure time of $t_{\text{exp}} = 320$ ms. Temperatures of the instrument were well within the nominal range ($T_{\text{detector}} = 236.33$ K and $T_{\text{optics}} = 276.83$ K), thus limiting the dark signal to less than 1 DN. The phase angle was 89.9°.

Unfortunately, the Apollo 16 landing site was close to the terminator during the observations resulting in a very low signal-to-noise ratio. We thus searched for a fully illuminated location (maximum signal about 2000 DN) with supposedly similar compositional characteristics to be taken as reasonable analogue. Our choice was a highland region close to Petavius and Langrenus craters and centered at longitude 318° and latitude −28°. We assumed that the observed reflectance at this point was equal to the spectrum of the Apollo 16 sample measured in the laboratory (Fig. 17); our assumption is based mainly on the fact that at the VIMS-V spatial resolution we observe a "mean" spectrum whose intensity variations over the lunar highland regions are mainly introduced by illumination angle (geometric effects). In Fig. 16 are shown the raw DNs for this location. (The sharp signal decrease at around 600 nm (band = 35) is due to the junction of the two order filters located on the CCD detector window.)

The instrument transfer function at the pixel corresponding to the above location on ground is given by:

$$\text{UR}(s^*, \lambda) = \frac{\text{DN}(s^*, \lambda)}{\rho_{\text{Moon}}(\lambda)\text{SR}(\lambda)t_{\text{exp}}}, \tag{2}$$

where $\rho_{\text{Moon}}(\lambda)$ is the spectral reflectance of the observed lunar location (for the corresponding illumination and viewing geometry) and $\text{UR}(s^*, \lambda)$ is transfer function corresponding to the spatial pixel s^*. The solar irradiance from (Thekaekara, 1973) has been adopted and converted to solar radiance $\text{SR}(\lambda)$ at the Sun–Moon distance. The Apollo 16 sample reflectance used is the one available in electronic form at the PDS node at the Brown University (Pieters, 1999), reported in Fig. 14.

It is well known that reflectance spectrum depends not only on the optical constants and the physical properties of the surface materials but also on the photometric geometry

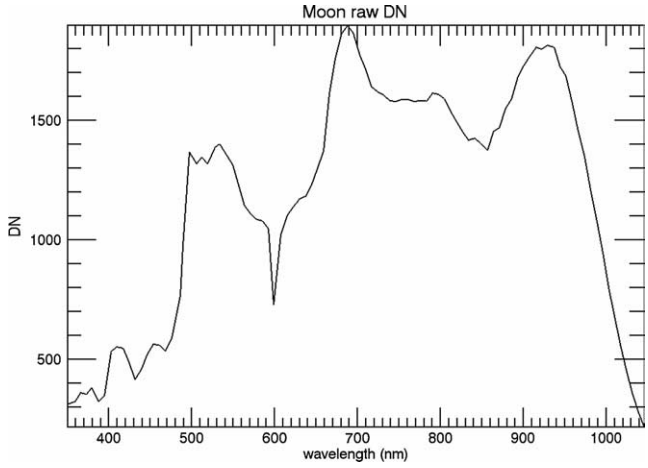

Fig. 16. Raw Moon DNs at the calibration point.

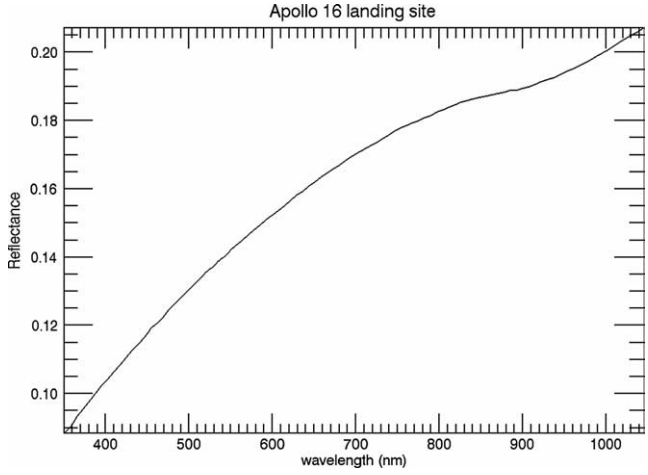

Fig. 17. Apollo 16 landing site sample reference spectrum. The measurement has been performed in the laboratory (after Pieters, 1999).

(Hapke, 1993) and the incidence, emission and phase angles. Several analytical relations have been proposed to take into account the illumination/observation geometry. The lunar spectral reflectance can be adequately described by a scattering law of the form (Gradie and Veverka, 1986):

$$\left(\frac{I}{F}\right)_{\lambda} = \frac{\mu_0}{\mu + \mu_0} A_{\lambda} f_{\lambda}(\alpha). \tag{3}$$

Where μ_0 and μ are the cosines of the incidence and emission angles, respectively, $A(\lambda)$ is a constant that depends on the absolute reflectance and $f(\alpha)$ is the phase function, which describes the variation of the reflectance as a function of the phase angle α. The spectral dependence of the reflectance on the phase angle has been known for a long time (Lane and Irvine, 1973) and shows a considerable reddening with increasing phase angle. We then compared the selected V-channel lunar spectrum taken at a phase angle of 90°, incidence of 62°, and emittance of 37.6°, with the laboratory measurement of an Apollo-16-landing-site sample taken at phase angle of 30°, incidence of 3° and emission of 0°.

From the disk-integrated photometric spectral measurements of Lane and Irvine (1973), which cover the wavelength range 359–1063 nm, we calculated the ratio between the Moon's brightness at the two phase angles (see Fig. 18). The Lane and Irvine data refer to disk-integrated measurements, hence they are a weighted average of the photometric properties of bright (highland) and dark (maria) terrains (Helfenstein and Veverka, 1987); this could be a potential source of error in the determination of the lunar reflectance as our selected spot refers to a highland region. Nevertheless, the Lane and Irvine data are the only spectrally resolved data available in the literature.

With these additional data we were able to calculate the proper value of the $\rho_{\text{Moon}}(\lambda)$ to be introduced in the expression for the UR(s,λ) given above. In Fig. 19 is shown the transfer function thus obtained at the slit center, while in Fig. 20 is shown the transfer function extended to the CCD frame. The UR shows a typical shape for CCD detectors with a maximum efficiency in the central spectral range and with a sharp fall at the extreme infrared edge; the order sorting filter is evident as a sharp absorption peak at band = 35. The reflectance $\rho_T(s,\lambda)$ of a generic target is then given by the expression:

$$\rho_T(s,\lambda) = \frac{\text{DN}_T(s,\lambda)}{\text{UR}(s,\lambda)\frac{\text{SR}_{\text{Earth}}(\lambda)}{D_T^2} t_{\exp T}}. \tag{4}$$

Where D_T is the heliocentric distance of the target in AU, and $\text{SR}_{\text{Earth}}(\lambda)$ the solar spectral radiance measured at the mean Earth–Sun distance (1 AU).

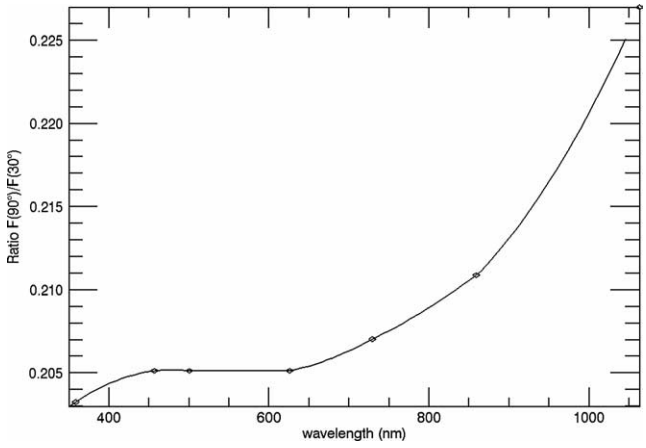

Fig. 18. Ratio between the Moon brightness at the two phase angles of 90° (VIMS-V observation) and 30° (laboratory measurement), as calculated from Lane and Irvine (1973) phase dependent spectral magnitudes.

5.5. *Comparison of Jupiter spectral albedo with ground based data*

The absolute reflectance of Jupiter as obtained from V-channel data during the C23 (Cruise 23) mission phase was then compared to data in the literature to verify the quality of the radiometric calibration. We used the cube V1355182709 acquired at 2000-345T23:27:02.463Z, which has an exposure time of 640 ms; the Cassini–Jupiter distance was of 20.847 million kilometers and the phase angle 3.6°.

The Jupiter disk resolved reflectance was transformed to full-disk reflectance, and compared to the Karkoschka (1994) telescopic data taken with a spectral resolution of 1 nm (note that the V channel has a spectral resolution in the nominal mode of 7.3 nm) and at a phase angle of 9.8°. The ground-based telescopic spectrum was resampled at the V wavelengths, and the comparison is shown in Fig. 21. At this stage we did not attempt to correct for the phase difference between the two spectra. The two spectra are shown at the bottom of Fig. 21 and the ratio of the two is shown in

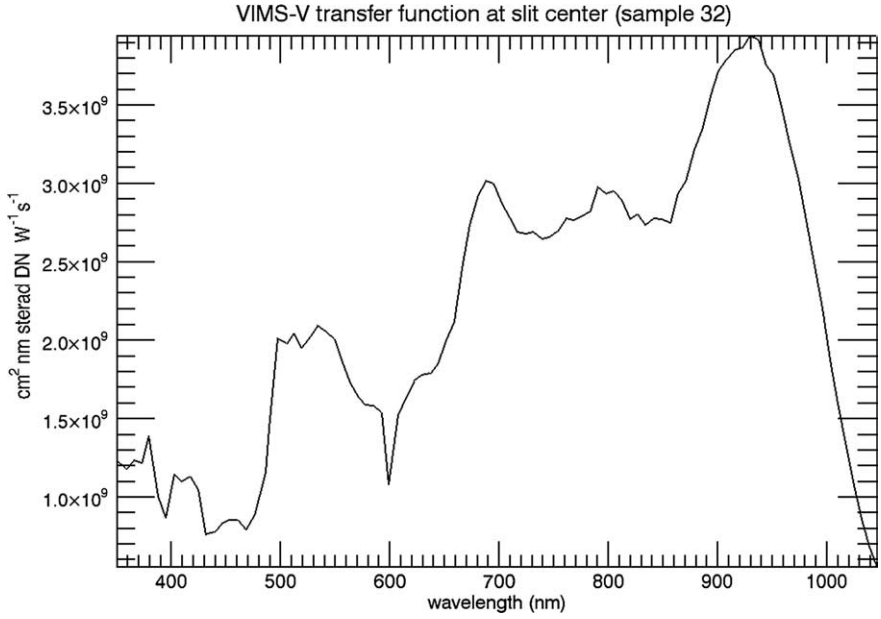

Fig. 19. VIMS-V spectral transfer function at slit's center (sample = 32).

the upper portion of the figure. The large variation at about 890 nm is due to the very low signal at the bottom of an almost saturated CH_4 absorption band. Also, at around 730 nm there is a relatively large peak that is most probably due to the incomplete correction of the spectral resolution of the two sets of data.

Removal of these variations results in an absolute calibration error of about 15%, which is not randomly distributed in the spectral range, but grows linearly from blue to red. We believe this is the result of an incomplete phase correction probably due to compositional differences between the Lane and Irvine (1973) Moon disk-integrated brightness data and the selected V observations. An additional source of error could be related to the spectral differences between the Apollo 16 sample spectral reflectance and the selected Petavius region.

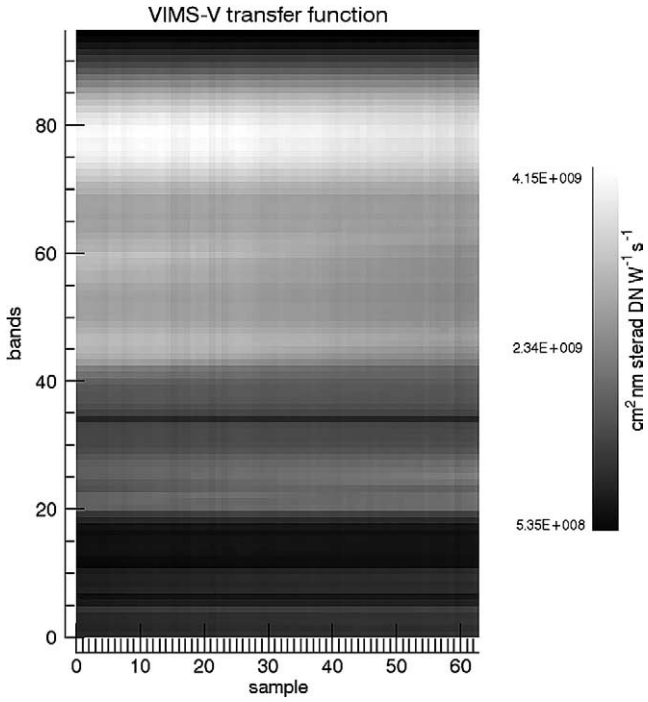

Fig. 20. VIMS-V transfer function over the frame (64 samples, 96 bands). The definition of the axes is the same as in Fig. 15.

6. Galilean satellite reflectance spectra analysis

6.1. Icy Ganymede and Europa

The reflection spectra of Ganymede and Europa (Fig. 12) are both dominated by the effects of water ice and hydrated materials (McCord et al., 1998a, 1998b, 1999, 2001, 2002; Hansen and McCord, 2004). Water ice and hydrated materials are bright in the near infrared, so the longer integration time observations of both Ganymede and Europa saturate at the short-wavelength end of the DN spectrum (left), but this is necessary to increase the signal for the 2.5–5-μm region. This effect is less extreme for less-icy Callisto (Fig. 12). The absorption bands at 1, 1.25, 1.5, 1.65, 2, and 2.8 μm are all due to the presence of H_2O and/or OH, as is the small Fresnel reflectance peak at 3.1 μm in the reflection of Ganymede, which cannot be seen in the VIMS spectra of Europa (Hansen and McCord, 2004). The reflection of water-bearing materials is low beyond 3 μm, which reduces the signal to less than 20 DN for Ganymede and less than 10 DN for Europa. Yet even with these extremely low signal levels, the CO_2 absorption band is easily detected for Ganymede and Callisto, and is likely there for Europa, where

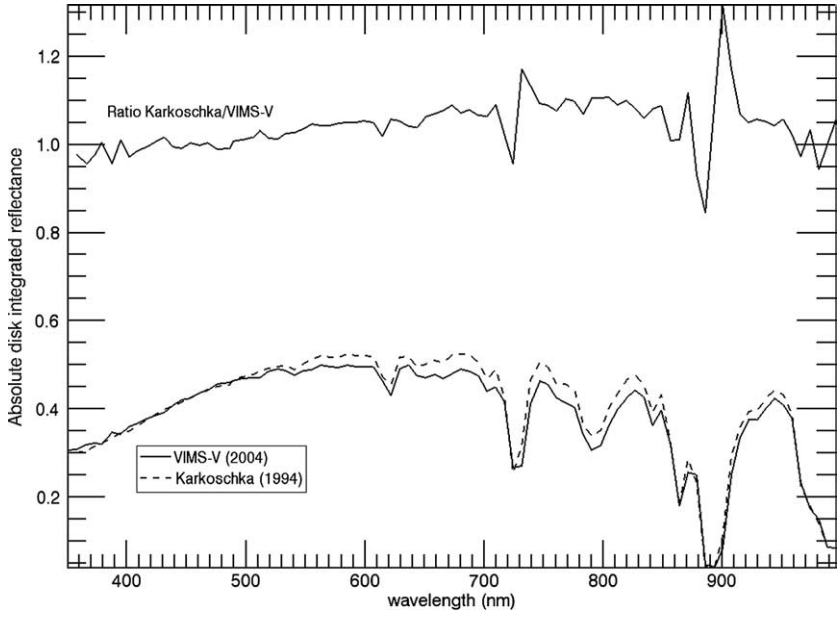

Fig. 21. Absolute disk integrated Jupiter reflectance evaluated by VIMS-V and by ground-based observations (Karkoschka, 1994). The main absorption features, due to methane and ammonia, are identified. The ratio between the two spectra is plotted in the upper part.

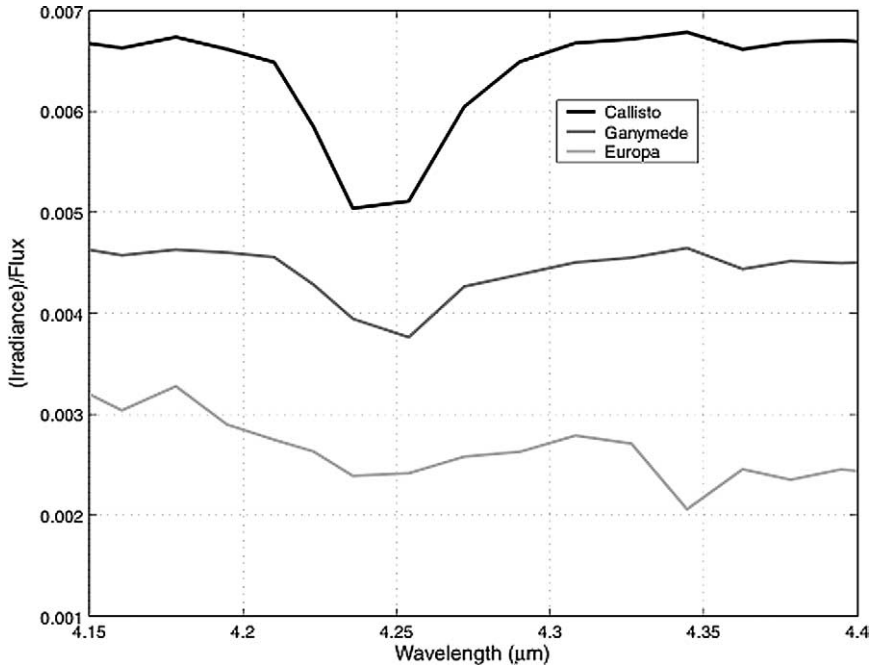

Fig. 22. The CO_2 absorption band in VIMS spectra of Callisto (black) and Ganymede (dark gray) are scaled for comparison with the probable CO_2 absorption band in VIMS spectrum of Europa. The multiple-channel nature of the Europa feature suggests it is not an artifact, and the shape is similar to that of the CO_2 feature on Ganymede. The single-channel features also present are likely artifacts. Note, the extremely low signal level at which this detection is made also equates to less than 10 DN (in an average of only 7 spectra).

the surface albedo is very low (Fig. 22). It is not possible to directly analyze the water of hydration absorptions separately from the water-ice features, especially near 1.45 and 1.95 μm, in the VIMS spectra for Europa and Ganymede. This is because the water of hydration features occur at specific areas on the surface that are not resolved by the VIMS observations of the anti-jovian hemisphere with an effective central longitude of 175° (Table 1). Thus, only a mix of water ice and hydrated minerals is present in VIMS spectra.

6.2. *Carbon dioxide and other minor constituents on Ganymede and Callisto and possibly Europa*

The CO_2 absorption band in the reflectance spectra of Callisto and Ganymede at ∼ 4.25 μm (Fig. 11) confirms the discovery of CO_2 from reflection spectra returned by the Galileo NIMS instrument. This absorption may also be present in VIMS spectra of Europa, as reported by NIMS (McCord et al., 1998a; Smythe et al., 1998), but the depth is similar to the one-channel, one-sigma error (Fig. 22). Additionally, a possible absorption in the NIMS spectra near 4.37 μm may also be present in the VIMS spectra at about the same strength, although more analysis to remove the patterns in the VIMS spectra is needed to determine this with certainty. If real, this feature is most likely due to the isotope ^{13}C. The SO_2 absorption bands are not well resolved in the VIMS spectrum of Callisto because this observation is of its trailing hemisphere where the absorption band is very weak (Hibbitts et al., 2000). However, the CN band at 4.57 μm is again detected on Callisto (Fig. 12), and its shape is similarly asymmetric relative to that derived by McCord et al. (1998a), although it is shallower than it usually appears in NIMS spectra, probably due to the VIMS hemispheric averaging of Callisto properties.

6.3. *Io spectrum*

After recalibration, we again compare the Io spectra from NIMS and VIMS (Fig. 23). The absorption-band positions now agree and the spectra have a similar shape. The long-wavelength portion of the VIMS spectrum has much greater signal than for NIMS. This is due to regions on Io with high-temperature volcanic activity being included within the VIMS observations

The eclipse observation of Io is centered on longitude 310° W and on Loki (309° W, 13° N) during the simultaneous Galileo spacecraft G29 observation of Loki by NIMS. The NIMS results suggest a two-temperature surface (2330 km^2 at 417 K, and 0.6 km^2 at 1085 K (Davies et al., 2001). We find (Fig. 24) that a very similar two-temperature curve also matches the radiance output determined by VIMS, which also includes the entire remaining hemisphere of Io. We chose one component to be the 2330 km^2 417 K surface. This requires a second warmer component ∼ 1105 K and 1.9 km^2 to match the observed radiance. The difference between the NIMS and VIMS observations could be due to the hemispheric nature of the VIMS observation and the inclusion of other hot spots.

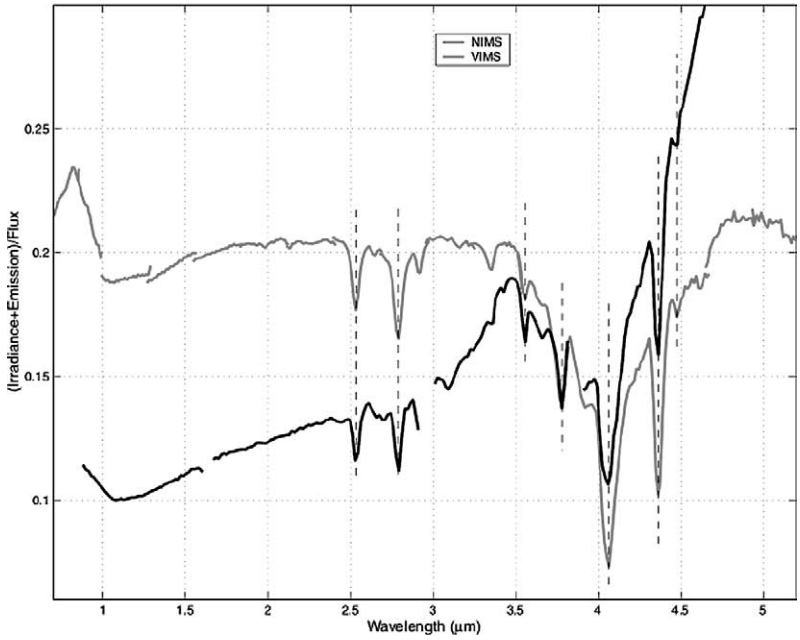

Fig. 23. The Io reflectance spectra from VIMS and NIMS are shown after the revised radiometric and spectral calibrations have been applied to the VIMS data. These results should be compared with those shown in Fig. 10.

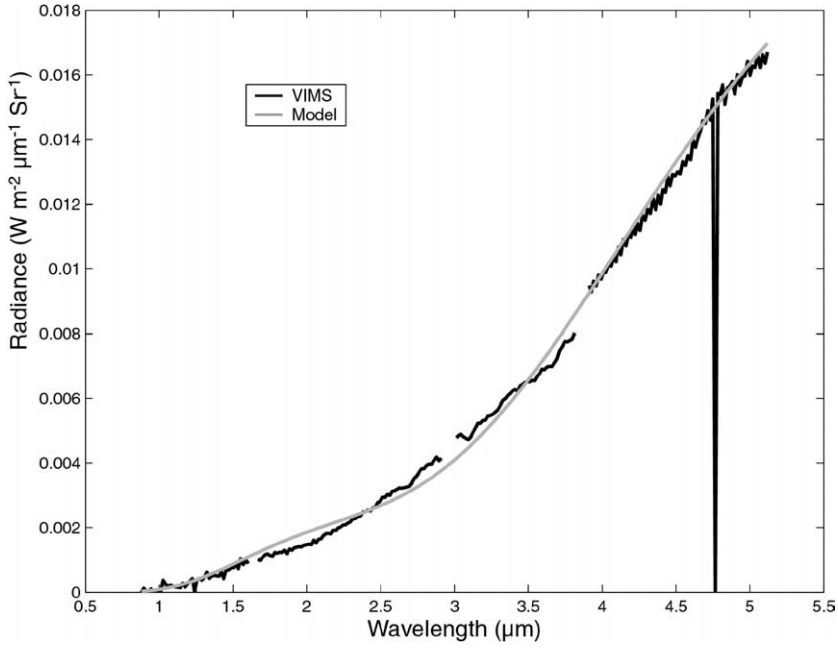

Fig. 24. VIMS IR spectrum for Io in eclipse and centered on the longitude of Loki shows a strong thermal component. A model spectrum consisting of two blackbody temperature contributions (2330 km^2 at 417 K and 1.9 km^2 at 1105 K) is also plotted.

6.4. Satellites spectral reflectances in the VIS channel

The V channel produced a large data set, but the amount of data could be misleading as the large variations in observing situations produced a large variation in the data quality. In particular, the serendipitous observations (such as those obtained with the satellite being caught inside the V frame while observing Jupiter) are mainly single cubes and spectral averaging is not possible. We also discarded all those cubes taken at distances such that the satellite angular size is sub-V slit (i.e., less than 167 μrad). Thus, we performed the spectral analysis using only the observations listed in Table 2.

All the observations were calibrated with the transfer function described in Section 5. Corrections were made for the geometry of the observation, according to the relation:

$$\rho_{\mathrm{CORR}}(\lambda) = \frac{\rho(\lambda)}{\mathrm{AR} \cdot \mathrm{PF}}, \tag{5}$$

where $\rho(\lambda)$ is the reflectance obtained after the radiometric calibration, AR is the ratio between the satellite area and the IFOV area (in nominal operation mode), and PF is the phase factor, which represent the fraction of the illuminated area of the satellite disk at the given phase angle.

Given the wide range of observing conditions and the low signal and DN values, we did not attempt to perform analyses of individual observations, but rather we used, wherever possible, averages of individual spectra. In Fig. 25 are shown the reflectances for all the satellites: Io is scaled to 1.0 at 563 nm, Europa to 0.8, Ganymede to 0.6, and Callisto to 0.4 to avoid superposition of spectra, and compared to telescopic observation obtained by Karkoschka (1994). Scaling is necessary because the averaged spectra represent a collection obtained over a wide range of phase angles (for instance, Europa and Ganymede phase changes of about 50°). Comparison of the VIMS V result with the Karkoschka telescopic observations shows general overall agreement but with several similar differences for all satellites, up to about 10% in magnitude. As for the Jupiter data, there is a consistent decrease in reflectance towards the IR (see Section 5.5). This suggests that an adjustment to the calibration function as derived before the Jupiter encounter is needed, and again illustrates the general approach to deriving a continuously improving radiometric calibration for the VIMS instrument.

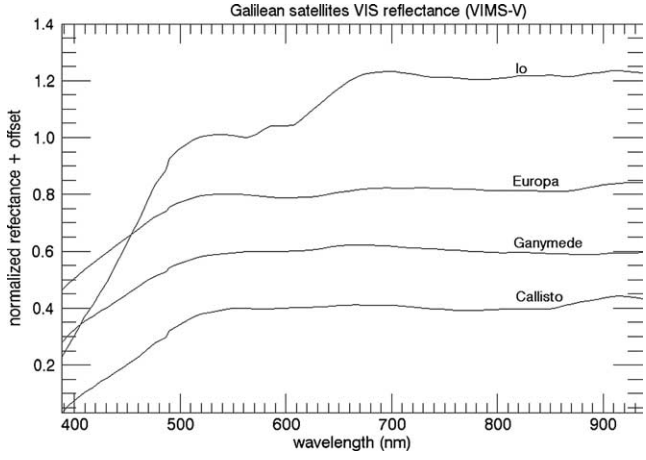

Fig. 25. Galilean satellites spectra: VIMS-V results (a) are compared with ground-based observations (Karkoschka, 1994), (b). Io spectrum is normalized to 1.0 at 563 nm, Europa at 0.8; Ganymede at 0.6; Callisto at 0.4.

The Io spectrum shows three interesting features, which can be correlated to its surface composition. The spectrum displays a steep rise with an 80% reflectance increase from 350 to about 500 nm. A plateau up to 600 nm and an additional rise, although with less slope, up to 700 nm. Longward of 700 nm the spectrum remains flat. A hint of an absorption feature, centered at about 350 nm, can be seen at the lower end of the spectrum.

All these features can be compared with the recent classification of Io surface materials performed by Geissler et al. (1999). They used Io disk-resolved images taken by the Galileo SSI (Solid State Imaging) system. They pointed out the presence of four distinct units characterized by distinct spectral properties in the Vis-NIR range and best distinguished by their spectral slopes: (1) Yellow material that covers about 40% of Io's surface, is concentrated mainly in the equatorial region and displays steep positive slopes from violet to green (400–550 nm); (2) Red material covering about 32% of the region above 30° latitude and displaying steep (but less steep than yellow materials) slopes from violet to red (350 through 750 nm); (3) White material that covers about 27% of Io's surface, is the brightest, and displays a shallow slope at short wavelengths up to 700 nm. Finally, there is dark material, covering 1% of the surface and showing a fairly flat spectrum, located at isolated spots and patches around the main calderas. All the observed features of Io have been correlated with sulfur and sulfur dioxide. Additionally, SO_2 frost is responsible for the minimum of an absorption band at around 350 nm. The V disk-integrated observations represent the convolution of these single unit spectra and effectively reproduce a composite Io spectrum showing all the spectral features seen by Galileo SSI.

6.5. *Satellite phase curves*

Cassini observations of the Jupiter satellites cover a wide range of phase angles: Europa from 0.4° to about 115°; Ganymede from 15° to 108°, and Callisto from 18° to 95°. Contrarily to what has been done for the spectral analysis, we have also used the lower SNR serendipitous observations, which, although of poor spectral quality, allow improvement of the phase angle coverage.

We show the resulting phase curves for absolute reflectances at 563 nm in Figs. 26, 27, and 28. In the same plot we have added (shown with a different symbol) the geometric albedo (absolute reflectance at zero phase angle) of the bodies as reported (Buratti, 1995, and references therein), thus effectively extending our phase coverage to zero phase for all three icy satellites.

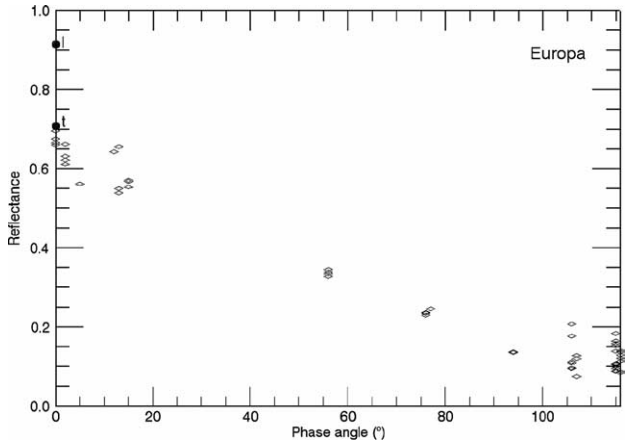

Fig. 26. Europa phase curve as derived by VIMS-V observations at a wavelength of 563 nm. The two large dots indicate the leading (l) and trailing (t) sides geometric albedo, 0.92 and 0.71, respectively (Buratti, 1995).

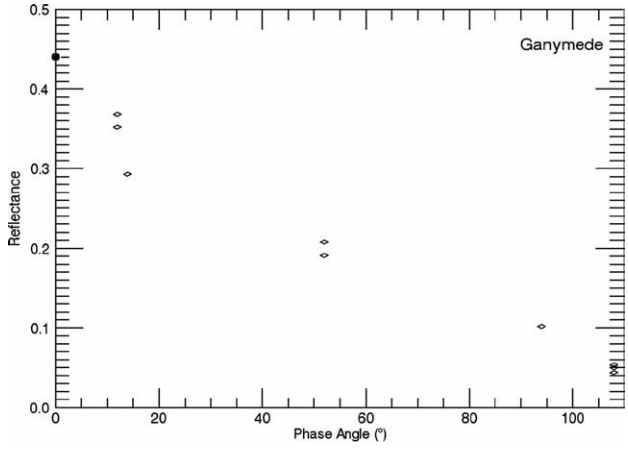

Fig. 27. Ganymede phase curve as derived by VIMS-V observations at 563 nm. The large dot at zero phase indicates the average leading-trailing geometric albedo (Buratti, 1995).

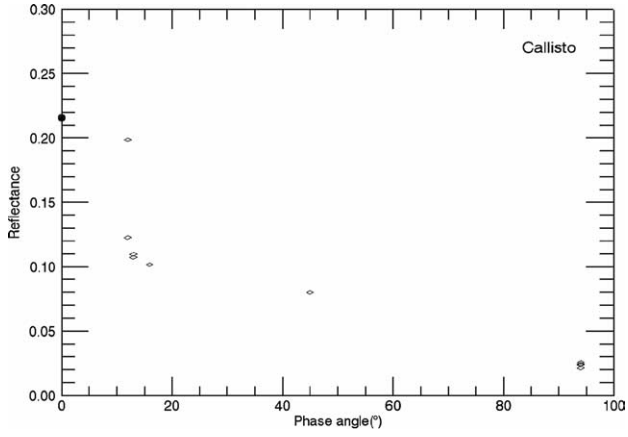

Fig. 28. Callisto phase curve as derived by VIMS-V observations at 563 nm. Large dot at zero phase indicates the average leading-trailing geometric albedo (Buratti, 1995).

We did not separate the observations according to their longitude, again to add more phase coverage but at the same time adding more scatter to the data. As a final consideration on the data quality, we point out that the data at both ends of the phase angle range for all the satellites were obtained at the beginning and the end of the close encounter phase when the distance between spacecraft and satellite was greatest and the SNR poorest.

Our data set for Europa slightly exceeds the Voyager phase angle coverage, while the Ganymede and Callisto coverage is more limited than for the Voyager data (Domingue and Verbiscer, 1997)

Europa has the largest geometric albedo variation between leading and trailing sides of all the satellites and the Europa trailing side displays an opposition surge while the leading one does not (Buratti and Golombeck, 1988). The VIMS data have a zero phase reflectance compatible with the trailing side albedo but they do not show an opposition surge. This mixed behavior could be explained by noting that almost all of the Europa observations used were centered on an intermediate longitude between the trailing and leading sides.

A complete description of the phase curve and of the surface's physical properties requires the calculation of a photometric model. We have not yet performed this analysis, However, the reflectance increase at about 120° is interesting as it points out the presence of a forward scattering component to the single particle scattering function, probably due to the overabundance of clear particles with respect to the internal scatterers, which would increase the backscattering component (Domingue et al., 1991; Domingue and Verbiscer, 1997). The Callisto phase curve (Fig. 28) shows, within the uncertainty due to the scattering of the data points, a more pronounced opposition surge than Ganymede (Fig. 27). Again this is compatible with previous analysis of Voyager data and subsequent modeling (Buratti, 1991).

Acknowledgments

This article resulted from a large amount of work and cooperation by the entire VIMS team that cannot be individually described here. In addition, we thank Larry Soderblom for the NIMS spectrum of Io shown in Fig. 8. This is University of Hawaii SOEST and HIGP publication numbers 6443 and 1342, respectively. The USA contribution was supported by the NASA Cassini Project VIMS Science Team budget. The Italian contribution was supported by an Italian Space Agency (ASI) grant.

References

Brown, R.H., Baines, K.H., Bellucci, G., Bibring, J.P., Buratti, B.J., Capaccioni, F., Cerroni, P., Clark, R.N., Coradini, A., Cruikshank, D.P., Drossart, P., Formisano, V., Jaumann, R., Langevin, Y., Matson, D.L., McCord, T.B., Mennella, V., Nelson, R.M., Nicholson, P.D., Sicardy,

B., Sotin, C., Amici, S., Chamberlain, M.A., Filacchione, G., Hansen, G.B., Hibbitts, C.A., Showalter, M., 2003. Observations with the visual and infrared mapping spectrometer (VIMS) during Cassini's flyby of Jupiter. Icarus 164, 461–470.

Brown, R.H., Baines, K.H., Bellucci, G., Bibring, J.P., Buratti, B.J., Bussoletti, E., Capaccioni, F., Cerroni, P., Clark, R.N., Coradini, A., Cruikshank, D.P., Drossart, P., Formisano, V., Jaumann, R., Langevin, Y., Matson, D.L., McCord, T.B., Mennella, V., Miller, E., Nelson, R.M., Nicholson, P.D., Sicardy, B., Sotin, C., 2004. The Cassini visual and infrared mapping spectrometer investigation. Space Sci. Rev. In press.

Buratti, B., Golombeck, M., 1988. Geologic implications of spectrophotometric measurements of Europa. Icarus 75, 437–449.

Buratti, B., 1991. Ganymede and Callisto: surface textural dichotomies and photometric analysis. Icarus 92, 312–323.

Buratti, B., 1995. Photometry and surface structure of the icy Galilean satellites. J. Geophys. Res. 100, 19061–19066.

Calvin, W.M., Clark, R.N., Brown, R.H., Spencer, J.R., 1995. Spectra of the icy Galilean satellites from 0.2 to 5 μm: a compilation, new observations, and a recent summary. J. Geophys. Res. 100, 19041–19048.

Capaccioni, F., Coradini, A., Cerroni, P., Amici, S., 1998. Imaging spectroscopy of Saturn and its satellites: VIMS-V onboard Cassini. Planet. Space Sci. 46 (9/10), 1263–1276.

Carlson, R.W., Weissman, P.R., Smythe, W.D., Mahoney, J.C., the NIMS Science and Engineering Teams, 1992. Near-infrared mapping spectrometer experiment on Galileo. Space Sci. Rev. 60, 457–502.

Carlson, R., Smythe, W., Baines, K.H., Barbinis, E., Becker, K., Burns, R., Calcutt, S., Calvin, W., Clark, R., Danielson, G., Davies, A., Drossart, P., Encrenaz, T., Fanale, F., Granahan, J., Hansen, G.B., Herrera, P., Hibbitts, C., Hui, J., Irwin, P., Johnson, T., Kamp, L., Kieffer, H., Leader, F., Lellouch, E., Lopes-Gautier, R., Matson, D.L., McCord, T.B., Mehlman, R., Ocampo, A., Orton, G., Roos-Serote, M., Segura, M., Shirley, J., Soderblom, L., Stevenson, A., Taylor, F., Torson, J., Weir, A., Weissman, P., 1996. Near-infrared spectroscopy and spectral mapping of Jupiter and the Galilean satellites: results from Galileo's initial orbit. Science 274, 385–388.

Clark, R.N., McCord, T.B., 1980. The Galilean satellites: new near-infrared spectral reflectance measurements (0.65–2.5 microns) and a 0.325–5 microns summary. Icarus 41, 323–339.

Coradini, A., Filacchione, G., Capaccioni, F., Cerroni, P., Ariani, A., Brown, B.H., Langevin, J., Gondet, B., 2004. INI-VIMS at Jupiter: radiometric calibration tests and data results. Planet. Space Sci. In press.

Davies, A.G., Radebaugh, J., Keszthelyi, L., McEwen, A., the Galileo NIMS Team, the Cassini SSI Team, 2001. Temperature-area determination from observations of Loki by Galileo and Cassini. In: AAS-DPS Annual Conference.

Domingue, D.L., Hapke, B.W., Lockwood, G.W., Thompson, D.T., 1991. Europa's phase curve: implications for surface structure. Icarus 90, 30–42.

Domingue, D.L., Verbiscer, A., 1997. Re-analysis of the solar phase curves of the icy Galilean satellites. Icarus 128, 49–74.

Geissler, P.E., McEwen, A.S., Keszthelyi, L., Lopes-Gautier, R., Granahan, J., Simonelli, D.P., 1999. Global color variation on Io. Icarus 140, 265–282.

Gradie, J., Veverka, J., 1986. Photometric properties of powdered sulphur. Icarus 58, 227–245.

Hansen, G., McCord, T.B., 2004. Amorphous and crystalline ice on the Galilean satellites: a balance between thermal and radiolytic processes. J. Geophys. Res. 109 (1). E01012.

Hapke, B., 1993. Theory of Reflectance and Emittance Spectroscopy. Cambridge Univ. Press, Cambridge, UK.

Helfenstein, P., Veverka, J., 1987. Photometric properties of lunar terrains derived from Hapke's equation. Icarus 72, 342–357.

Hibbitts, C.A., McCord, T.B., Hansen, G.B., 2000. Distribution of CO_2 and SO_2 on the surface of Callisto. J. Geophys. Res. 105, 22541–22558.

Hibbitts, C.A., Pappalardo, R.T., Hansen, G.B., McCord, T.B., 2003. Carbon dioxide on Ganymede. J. Geophys. Res. 108, 5036.

Karkoschka, E., 1994. Spectrophotometry of the jovian planets and Titan at 300–1000 nm wavelength: the methane spectrum. Icarus 111, 174–192.

Lane, A.P., Irvine, W.M., 1973. Monochromatic phase curves and albedos for the lunar disk. Astron. J. 78, 267–277.

McCord, T., Clark, R.N., Ray Hawke, B., McFadden, L.A., Owensby, P.D., 1981. Moon: near-infrared spectral reflectance, a first good look. J. Geophys. Res. 86, 10883–10892.

McCord, T.B., Carlson, R.W., Smythe, W.D., Hansen, G.B., Clark, R.N., Hibbitts, C.A., Fanale, F.P., Granahan, J.C., Segura, M., Matson, D.L., Johnson, T.V., Martin, P.D., 1997. Organics and other molecules in the surfaces of Callisto and Ganymede. Science 278, 271–275.

McCord, T.B., Hansen, G.B., Clark, R.N., Martin, P.D., Hibbitts, C.A., Fanale, F.P., Granahan, J.C., Segura, M., Matson, D.L., Johnson, T.V., Carlson, R.W., Smythe, W.D., Danielson, G.E., the NIMS Team, 1998a. Non-water-ice constituents in the surface material of the icy Galilean satellites from the Galileo near infrared mapping spectrometer investigation. J. Geophys. Res. 103, 8603–8626.

McCord, T.B., Hansen, G.B., Fanale, F.P., Carlson, R.W., Matson, D.L., Johnson, T.V., Smythe, W.D., Crowley, J.K., Martin, P.D., Ocampo, A., Hibbitts, C.A., Granahan, J.C., the NIMS Team, 1998b. Salts on Europa's surface detected by Galileo's near infrared mapping spectrometer. Science 280, 1242–1245.

McCord, T.B., Hansen, G.B., Matson, D.L., Johnson, T.V., Crowley, J.K., Fanale, F.P., Carlson, R.W., Smythe, W.D., Martin, P.D., Hibbitts, C.A., Granahan, J.C., Ocampo, A., the NIMS Team, 1999. Hydrated salt minerals on Europa's surface from the Galileo NIMS investigation. J. Geophys. Res. 104, 11827–11851.

McCord, T.B., Hansen, G.B., Hibbitts, C.A., 2001. Hydrated salt minerals on Ganymede's surface: evidence of an ocean below. Science 292, 1523–1525.

McCord, T.B., Teeter, G., Hansen, G.B., Sieger, M.T., Orlando, T.M., 2002. Brines exposed to Europa surface conditions. J. Geophys. Res. 107, 4–1.

McEwen, A.S., 1996. A precise lunar photometric function. In: Proc. Lunar Planet. Sci. Conf. 27th, p. 841.

Murchie, S., Robinson, M., Hawkins III, S.E., Harch, A., Helfenstein, P., Thomas, P., Peacock, K., Owen, W., Heyler, G., Murphy, P., Darlington, E.H., Keeney, A., Gold, R., Clark, B., Izenberg, N., Bell III, J.F., Merline, W., Veverka, J., 1999. Inflight calibration of the NEAR multispectral imager. Icarus 140, 66–91.

Pieters, C.M., 1999. The Moon as a spectral calibration standard enabled by lunar samples: the Clementine example. In: Workshop on New Views of the Moon II: Understanding the Moon Through the Integration of Diverse Datasets, Flagstaff, AZ. Abstract 8025.

Smythe, W.D., Carlson, R.W., Ocampo, A., Matson, D., Johnson, T.V., McCord, T.B., Hansen, G.B., Soderblom, L.A., Clark, R.N., 1998. Absorption bands in the spectrum of Europa detected by the Galileo NIMS instrument. In: Proc. Lunar Planet. Sci. Conf. 29th, Houston, TX, March 16–20. Abstract 1532.

Thekaekara, M.P., 1973. Solar energy motion in space (SEMIS). In: Proc. Symp. Solar Radiation Meas. and Instrumentation, pp. 414–442. SEE N76-15973 06-92.